International Communications in Heat and Mass Transfer 178 (2026) 111842

Contents lists available at ScienceDirect

International Communications in Heat and Mass Transfer

journal homepage: www.elsevier.com/locate/ichmt

Multi-objective artificial neural network-genetic algorithm optimization of transient thermal storage device in a hexagonal phase change material system

Yonghui Li [a], Ali Basem [b], Haibo Zhang [a,*], Mohamed Arbi Khlifi [c,**], Hyder H. Abed Balla [d,***], Mohammad Nadeem Khan [e], Hanaa Abu-Zinadah [f], Farkhod Rakhmonov [g], Yasser Fouad [h,****], Ibrahim Mahariq [i,j,k,*****]

[a] School of Digital Economy and Management, Sichuan Technology and Business University, Meishan, Sichuan 620000, China
[b] Advanced Technical College, University of Warith Al-Anbiyaa, Karbala, Iraq
[c] Department of Electrical Engineering, Faculty of Engineering, Islamic University of Madinah, Madinah 42351, Saudi Arabia
[d] Aeronautical Technical department, Najaf Technical Institute, Al Furat Al Awsat Technical University, Najaf, Kufa, Iraq
[e] Department of Mechanical and Industrial Engineering, College of Engineering, Majmaah University, Al-Majmaah 11952, Saudi Arabia
[f] Department of Mathematics and Statistics, College of Science, University of Jeddah, Jeddah, Saudi Arabia
[g] School of Exact Sciences, National Pedagogical University of Uzbekistan Named after Nizami, Uzbekistan
[h] Department of Applied Mechanical Engineering, College of Applied Engineering, Muzahimiyah Branch, King Saud University, P.O. Box 800, Riyadh 11421, Saudi Arabia
[i] Department of Electrical and Electronic Engineering, Faculty of Engineering and Architecture, Istanbul Gelisim University, Avcılar 34310, Istanbul, Türkiye
[j] Department of Medical Research, China Medical University Hospital, China Medical University, Taichung, Taiwan
[k] University College, Korea University, Seoul 02481, South Korea

ARTICLE INFO

Keywords:
Thermal energy storage
Multi-objective optimization
Artificial neural network
Genetic algorithm
Pareto front analysis
Phase change material

ABSTRACT

Latent thermal energy storage systems based on phase change materials (PCMs) play a vital role in improving energy efficiency, mitigating peak thermal loads, and facilitating the integration of renewable energy sources. Their ability to store large amounts of heat within a narrow temperature range makes them particularly attractive for applications in solar energy systems, waste heat recovery, and thermal management technologies. Nevertheless, the inherently low heat-conduction of most PCMs significantly limits charging rates, thereby restricting their practical performance. In response to these challenges, this work introduces a novel hexagonal thermal energy storage device inspired by honeycomb architectures and conventional shell-and-tube heat exchangers. The design integrates two concentric hexagonal frameworks within a unified outer shell, interconnected by structural bases rather than conventional fins. This monolithic configuration not only increases the effective heat-transfer surface but also creates extended conductive pathways that accelerate melting during charging cycles. The segmented internal domain further enables the use of multiple PCMs to meet varying thermal demands, while improving mechanical integrity and reducing leakage risks. To identify the optimal configuration for maximum energy storage, an artificial neural network predictive model is coupled with a multi-objective genetic algorithm, with the first and second hexagon lengths and the system inclination angle as key design variables. Two distinct optimal cases were identified by single-objective optimization (Optimal Cases 1 and 2). Another optimal case was derived from multi-objective optimization and the TOPSIS method, referred to as Optimal Case 3. By 5 h, all three optimized cases had fully melted (liquid fraction = 1). In contrast, the Core Case exhibited significantly slower melting behavior with the liquid fraction of 0.505. Besides, the optimized

* Corresponding author.
** Corresponding author.
*** Corresponding authors.
**** Corresponding author.
***** Corresponding author at: Department of Electrical and Electronic Engineering, Faculty of Engineering and Architecture, Istanbul Gelisim University, Avcılar 34310, Istanbul, Türkiye.
E-mail addresses: yjy848@126.com (H. Zhang), medarbi@iu.edu.sa (M.A. Khlifi), hyderballa@atu.edu.iq (H.H. Abed Balla), yfouad@ksu.edu.sa (Y. Fouad), lbmmahariq@gmail.com (I. Mahariq).

https://doi.org/10.1016/j.icheatmasstransfer.2026.111842

Available online 3 July 2026

cases stored about 13,500 kJ of thermal energy, while the Core Case reached only 7621 kJ. Compared to the Core Case, the improvements remained significant, at approximately 77.5%.

Nomenclature

C_p	specific heat (J/kg·K)
D	characteristic height (m)
E_m	melting enhancement ratio (%)
F	latent enthalpy of melting (J/kg)
FL	length of the first hexagon (mm)
g	gravitational acceleration (m/s^2)
ΔH	latent enthalpy (J/kg)
H	specific enthalpy (J/kg)
k	thermal conductivity (W/m·k)
M_f	mushy region parameter
P	pressure (Pa)
Ra	Rayleigh number
S	source term
SL	length of the second hexagon (mm)
t	time (s)
T	temperature (K)
V	velocity (m/s)
θ	inclination angle of the system (degree)
ε	small numerical constant
φ	liquid fraction
β	coefficient of thermal expansion (1/K)
ρ	density (kg/m^3)
μ	dynamics viscosity (kg/m·s)

Abbreviations

ANN	artificial neural networks
GA	genetic algorithm
OpC	optimal case
RMSE	root mean square error
TSD	thermal storage device

1. Introduction

Solar radiation represents the most abundant and geographically distributed renewable energy source, delivering orders of magnitude more energy to the Earth's surface than current global demand [1]. However, its practical exploitation fluctuates on daily and seasonal scales and is strongly influenced by weather conditions and location [2]. This inherent variability creates a temporal mismatch between energy availability and end-use requirements. As a result, a significant fraction of the harvested thermal energy cannot be utilized directly, limiting system efficiency and reliability [3]. Thermal storage devices (TSDs) offer an effective solution by enabling the accumulation and controlled release of solar-derived heat. This capability stabilizes energy supply and expands the integration of solar thermal technologies across power generation, industrial processes, and building energy systems [4].

TSDs are commonly classified into thermochemical, sensible, and latent storage types according to the physical processes governing energy storage [5]. Thermochemical storage exploits reversible chemical reactions to achieve high theoretical energy density and minimal thermal losses. Sensible thermal storage relies on temperature variation within a storage medium and is characterized by simple design and low cost [6]. In contrast, latent thermal energy storage has attracted considerable attention because it utilizes phase change materials (PCMs) to achieve high energy-storage density within a narrow temperature range. PCMs are widely recognized for their ability to absorb and store large amounts of heat within a narrow temperature range, making them highly suitable for maintaining temperature stability in sensitive systems [7]. In battery applications, especially in lithium-ion battery packs, PCMs are used to mitigate temperature rise, prevent thermal runaway, and enhance operational safety and lifespan [8]. Similarly, in electronic devices, PCMs are employed to manage transient heat loads, reduce temperature fluctuations, and improve the reliability of components such as CPUs, power electronics, and microprocessors [9]. PCMs absorb excess heat during charging via a solid-liquid transition and release the accumulated energy during discharge as the material solidifies. However, the full potential of PCM-based TSDs is hindered by their poor thermal conductivity [10]. Typical organic PCMs, such as paraffins and fatty acids, have thermal conductivities of 0.2–0.3 W·m^{-1}·K^{-1}, whereas many inorganic salt hydrates also exhibit insufficient heat transfer capability [11].

Approaches to improve the thermal behavior of PCMs fall into two main directions. Some efforts concentrate on manipulating the thermophysical properties of the PCM itself, while others aim to optimize heat exchange by redesigning the surrounding storage configuration [12]. Material-oriented developments are based on the formation of composite PCMs by incorporating highly conductive constituents or engineered fillers [13]. In contrast, configuration-oriented solutions focus on facilitating heat transfer between the PCM and the heat source [14]. This objective can be achieved through encapsulated layouts, conductive frameworks, and internal heat-spreading components that improve heat distribution within the storage unit [15]. Among structural solutions, properly designed internal elements, such as finned inserts or embedded channel networks, can shorten heat-diffusion paths, improve temperature uniformity, and enhance overall energy exchange. Numerous studies have investigated the influence of conductive enhancements on the thermal performance of PCM systems. Yang et al. [16] designed honeycomb-shaped fins for use in a thermal storage system. The effects of the fin thickness ratio and the number of layers on PCM discharge were evaluated. The simulation considered a three-layer configuration with a thickness ratio of 1:1:1 as the reference case. The data indicated that a six-layer finned unit enhanced the average heat transfer rate by 30%, but reduced fin efficiency by 8.1%. In addition, an optimized fin thickness ratio of 3:2:1 increased the heat transfer rate by 14% and decreased the discharging period by 12.7%. Tang et al. [17] combined longitudinal and twisted fin structures to maximize heat transfer performance in a latent TSD. The outcomes demonstrated that the composite setup accelerated melting time by up to 32.57% and solidification duration by 23.05% compared with longitudinal fins. It was also concluded that when 95% of the PCM was melted, the charging and discharging capacities were 10.9% and 3.4% higher than those achieved with annular fins. Pal et al. [18] examined the influence of fin configuration on PCM melting behavior by varying fin length and angular orientation. Fin lengths of 6.25 mm, 9.375 mm, and 12.5 mm were examined at inclination angles of 20°, 40°, 60°, and 80°. The findings revealed that the maximum reductions achieved were 31.13% for 80° fins at 6.25 mm, 37.12% for 40° and 80° fins at 9.375 mm, and 41.31% for 80° fins at 12.5 mm. Kamkari et al. [19] analyzed a TSD equipped with a biomimetic fractal-fin heat exchanger to evaluate thermal performance. The authors employed a conventional planar-fin exchanger as a baseline to isolate the influence of fin design. Compared with planar fins, the novel structure increased energy absorption and release powers

by up to 50% and 67%, respectively, while the corresponding times decreased by 37% and 44%, respectively. Benlekkam et al. [20] developed a series of Y-shaped fins to ameliorate the charging characteristics of RT35 PCM. By changing the branch angle, trunk length, and fin number, they identified an optimal geometry with a 2 mm trunk and a 60° branch angle. Although increasing the number of fins accelerated melting, it also increased material consumption. An optimized configuration reduced fin material by 23%, achieved a charging power of 74 W, and shortened the melting time by more than 20%.

The growing complexity of PCM-based TSDs has motivated the adoption of data-driven modeling techniques to predict their thermal capabilities [21]. Artificial neural networks (ANNs) have emerged as one of the most promising data-driven tools for addressing these challenges [22]. ANN-based frameworks are increasingly employed in recent literature to analyze and optimize the performance of TSDs. Liu et al. [23] utilized an ANN model to improve the power density of a finned storage unit operating under coupled charging and discharging conditions. The prediction model captured the combined influence of fin thickness, fin height, and PCM fraction on system performance. The trained ANN demonstrated acceptable accuracy, achieving an R^2 of 0.9979 and an RMSE of 0.295. The arrangement with optimal parameters achieved a power density of 95.62 kW/m3, representing a 29.71% improvement over the reference configuration. Mao et al. [24] employed ANNs to identify a structure that accelerates energy absorption in a triangular-rib-enhanced TSD. Two separate networks were designed to estimate the charging period at PCM liquid fractions of 0.5 and 1. The results indicated that the ANN-based models achieved high accuracy, with R^2 values of 0.996 and 0.992 for half- and complete-melting, respectively. The optimized setup enabled 100% PCM melting within 5 h, while the system without ribs reached a liquid fraction of 0.48 in the same time frame.

The proposed geometry is inspired by honeycomb architectures because of their excellent heat-transfer characteristics and high mechanical strength. These characteristics make such structures particularly suitable for thermal and industrial applications. In addition, the overall concept is influenced by conventional plate and shell-and-tube heat exchangers, where the HTF is distributed through tubes from an inlet manifold and collected at the outlet. However, unlike traditional shell-and-tube configurations, where tubes are typically fixed onto tube sheets and remain structurally independent from the shell, the proposed design introduces a fully integrated (monolithic) container in which the tubes are linked to the shell via internal bases. These bases perform multiple functions: they enhance heat transfer in a manner similar to fins, compensate for the low thermal conductivity of the PCM, improve structural integrity, and increase resistance to mechanical stresses. Moreover, they divide the internal container into interconnected regions, enabling the potential use of multiple PCMs with different melting temperatures within a single system, depending on application requirements. This multi-functionality of the internal structure distinguishes the present design from conventional geometries. From a practical standpoint, the system is also designed with manufacturability and operation in mind. The front and rear sections can be opened, facilitating maintenance, sediment removal from HTF channels, and PCM replacement. The modular nature of the container further allows multiple units to be arranged in series to increase storage capacity. Additionally, the integrated structure improves transportability and reduces leakage risks compared to multi-component assemblies. Regarding the investigated parameters, the selected design variables (*FL*, *SL*, and θ) are not arbitrary but physically meaningful. The length of the second hexagon (*SL*) directly influences both the heat transfer surfaces and the spatial configuration of the HTF tubes, determining whether they are located nearer to the core or the outer walls. The length of the first hexagon (*FL*) controls the distribution density of conductive pathways within the system. The inclination angle (θ) influences the intensity of buoyancy-driven natural convection, which plays a critical role in PCM melting. Beyond the geometric aspects, the primary contribution of this study lies in integrating this structured design with an ANN–GA-based optimization framework. The developed ANN predictive model serves as a fast and reliable surrogate, capable of estimating the system's energy absorption performance at different charging times without requiring repeated numerical simulations. This is particularly valuable given the complexity of the geometric parameters and their nonlinear interactions. In addition to optimization, the model also enables sensitivity analysis, offering deeper insight into the relative importance of design variables. Therefore, the main novelty of this work lies not only in the hexagonal configuration itself but also in its integration with an ANN–GA-based predictive and optimization framework.

2. Layout of the hexagonal PCM-based TSD

The general view of the device under study is depicted in Fig. 1a. The system consists of three concentric hexagonal containers with a total length of 800 mm, sealed at both ends using dedicated covers. The covers prevent PCM leakage during repeated phase transitions and reduce axial heat losses. These also act as HTF collectors inside the tubes. Based on the figure, the high-temperature HTF flows through the embedded tubes at the inlet and transfers thermal energy to the surrounding PCM (RT50 used in this research). The absorbed heat induces melting and enables energy storage as latent heat. A defining feature of the design is the presence of internal bases, which serve multiple functional roles. From a thermal perspective, they are arranged to compensate for the PCM's low thermal conductivity. Central PCM regions often suffer from delayed melting or solidification due to limited heat penetration. The bases augment the effective conduction areas from the shell and HTF tubes into the core of the container. Their geometry is specifically optimized to interact with both conduction and buoyancy-driven convection. Beyond heat transfer enhancement and the functionality of conventional fins, the bases also contribute to the mechanical integrity of the system. By rigidly connecting the hexagonal frames, they improve structural stability and help maintain precise alignment of internal elements. The bases and the shells of the PCM containers are manufactured from aluminum. Copper is indeed known for its superior thermal conductivity and lower thermal resistance compared to aluminum, which can enhance heat transfer performance. However, in the present study, aluminum is selected as the construction material due to several practical and engineering considerations. Firstly, copper has a significantly higher density, which results in a greater mass per unit volume. Consequently, devices made of copper are considerably heavier than those made of aluminum. This increased weight can negatively affect the ease of handling, installation, and structural integration of thermal energy storage systems, particularly in large-scale or portable applications. Secondly, copper is substantially more expensive than aluminum. From an economic standpoint, the use of copper would increase the overall cost of the system, making it less attractive for practical and commercial applications. In contrast, aluminum offers a favorable balance between thermal performance, weight, and cost, making it a widely used material in thermal management systems. The detailed computational domain, including geometrical specifications, is shown in Fig. 1b. Different colors have been assigned to each hexagonal layer to clearly indicate their roles: the first hexagon is shown in green, the second hexagon in blue, and the third (outer) hexagon in red. Additionally, the bases connecting the hexagonal layers are highlighted in gray, making their position and structural function more apparent.

Overall, the proposed geometry is based on a deliberately engineered configuration consisting of three concentric hexagonal layers that are structurally interconnected through bases. This design is not random; rather, it is systematically developed to enhance conductive pathways and promote buoyancy-driven heat transfer within the PCM domain. It is important to distinguish this structure from Voronoi geometries, which are typically microscopic porous structures formed through stochastic or natural partitioning processes. Voronoi structures are generally characterized by irregular, non-uniform cells that emerge in a non-

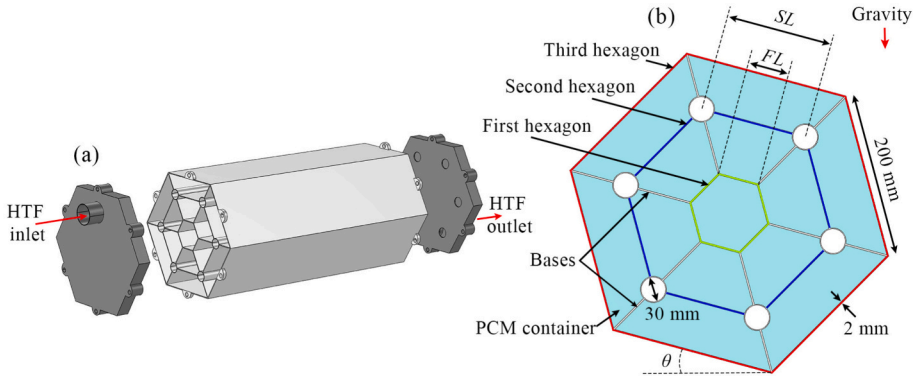

Fig. 1. (a) Schematic illustration of the proposed hexagonal thermal storage unit. (b) Cross-sectional view highlighting the geometric arrangement of concentric hexagonal structures and the PCM container.

engineered and often accidental manner, especially in porous media or topology optimization studies. While such structures may exhibit unique flow and thermal characteristics, they fundamentally differ from the present design in both scale and purpose. The current system is a macroscale, intentionally designed thermal storage configuration, whereas Voronoi structures are usually random, porous networks used for different applications such as lightweight materials or flow mixing enhancement. In this work, the HTF flows exclusively inside smooth, empty tubes, without any internal fins, porous media, or Voronoi-like structures. Therefore, the internal flow characteristics remain simple and consistent across all cases. Moreover, the PCM is enclosed within a sealed container and does not experience any forced flow in the longitudinal direction. Instead, heat transfer within the PCM is governed by a combination of conduction and natural convection (thermosyphon effect) driven by temperature gradients and buoyancy forces. As a result, no external pressure gradient is imposed on the PCM domain, and pressure drop within the PCM is not a governing parameter in this study. Additionally, the HTF operating conditions, including inlet velocity and pressure drop, are kept identical for all configurations. This ensures that any observed enhancement in thermal performance is solely attributed to geometric modifications within the PCM domain, rather than changes in flow conditions.

3. Enthalpy-porosity method for PCM numerical modeling

Phase change behavior in the PCM domain is commonly simulated applying the enthalpy-porosity formulation. Here, the solid-liquid interface is not tracked explicitly. Instead, the local phase state is characterized by a liquid fraction that evolves continuously from 0 in the solid phase to 1 in the fully liquid state. Cells with intermediate liquid fraction define the so-called mushy zone, where solid and liquid coexist. This region is modeled as a porous medium by introducing a momentum-damping source term that progressively restricts fluid motion as solidification proceeds. Such a treatment ensures numerical stability while preserving the physical coupling between heat transfer and natural convection. Owing to the flexibility of the enthalpy-porosity method, it is well-suited for systems involving complex geometries and strongly transient thermal conditions. To make the governing equations solvable, the following standard assumptions are adopted:

1. The molten PCM is considered an incompressible Newtonian fluid.
2. A 2D transient model is applied to describe heat transfer and fluid flow within the storage unit.
3. Both solid and liquid phases are assumed to be homogeneous and isotropic.
4. Buoyancy-driven flow is modeled using the Boussinesq approximation.
5. A uniform gravitational acceleration of 9.81 m s^{-2} is fixed in the downward vertical direction.
6. The flow inside the PCM container remains in the laminar regime, as the evaluated Rayleigh number does not exceed 10^9.
7. Energy dissipation due to viscous effects is neglected.
8. Constant thermophysical properties are assumed for both the PCM and structural materials, with the exception of density variation in the Boussinesq term to account for buoyancy effects. The corresponding values are compiled in Table 1.

This assumption is primarily justified by the narrow operating temperature range of the system. Specifically, the PCM used (RT50) undergoes phase change around 321.15 K, while the maximum temperature imposed by the HTF is 333.15 K. Therefore, the effective temperature variation during the melting process is around 12 K. Within such a limited temperature range, the thermophysical properties of the liquid PCM (such as thermal conductivity and specific heat) exhibit relatively minor variations, and their impact on the overall heat transfer behavior is limited. Moreover, this assumption is consistent with a large number of published studies on paraffin-based PCMs, where constant properties are commonly adopted to simplify the numerical model without significantly compromising accuracy [25]. For materials such as RT50, the data reported in the literature show that the thermophysical properties of the solid and liquid phases are relatively close, allowing properties like specific heat and thermal conductivity to be reasonably approximated as constant values within the studied temperature range. It is also important to note that the dominant physics in this study are governed by phase change and natural convection, which are primarily driven by latent heat and buoyancy effects. These mechanisms are already captured in the model through the enthalpy method and Boussinesq approximation. Nevertheless, it is acknowledged that incorporating temperature-dependent properties could further improve model fidelity, particularly for wider temperature ranges or different PCM types. This is considered as a limitation of the study and suggested as a direction for future research. Overall, the assumption of constant properties in this work provides a reasonable balance between

Table 1
The corresponding values of material properties.

Properties	RT50 [26]		Aluminum [27]
	Solid	Liquid	
ρ (kg/m^3)	880	760	2719
C_p (J/kg·K)	2000	2000	871
k (W/m·K)	0.2	0.2	202.4
μ (kg/m·s)	–	0.0038	–
β (1/K)	0.0006		–
F (J/kg)	168,000		–
T_m (K)	318.15–324.15		–

computational efficiency and accuracy and does not significantly affect the reliability of the presented results.

4. Mathematical procedure

4.1. Governing equations

The Rayleigh number (Ra) is defined using the gravitational acceleration (g), thermal expansion coefficient (β), specific heat capacity (C_p), density (ρ), characteristic length (D), dynamic viscosity (μ), and thermal conductivity (k) [28].

$$Ra = \frac{g\beta C_p \rho^2 (T_{HTF} - T_{PCM}) D^3}{\mu k} \tag{1}$$

The continuity equation enforces mass conservation for the incompressible PCM, as written in Eq. (2) [29]:

$$\rho_{0,l}(\nabla . V) = 0 \tag{2}$$

The divergence of the velocity field (V) is zero, ensuring that density variations are neglected except where they contribute to buoyancy through the Boussinesq approximation. The momentum balance given in Eq. (3) captures the interaction between fluid motion and phase transition.

$$\rho_{0,l}\left(\frac{\partial V}{\partial t} + V.\nabla V\right) = -\nabla P + \mu\nabla^2 V + g\rho_{0,l}(1 - \beta(T - T_0)) + S \tag{3}$$

The parameter T_0 in Eq. (3) represents the reference temperature used in the Boussinesq approximation, and in the present study it is taken as 298.15 K. This value corresponds to the initial uniform temperature of the system. The source term (S) represents the Darcy-type damping force introduced by the enthalpy-porosity method, which suppresses velocity in regions undergoing solidification. The energy relations for the liquid and solid domains are expressed in Eqs. (4) and (5), respectively [30]:

$$\rho_{0,l}\left(\frac{\partial H}{\partial t} + V.\nabla H\right) = k_l \nabla^2 T \tag{4}$$

$$\rho_s \frac{\partial H}{\partial t} = k_s \nabla^2 T \tag{5}$$

The PCM total enthalpy (H) can be evaluated by Eq. (6) [31]:

$$H = h + \Delta H \tag{6}$$

The sensible enthalpy component (h) is calculated in the following manner [32]:

$$h = h_{ref} + \int_{T_{ref}}^{T} C_p dT \tag{7}$$

The latent enthalpy (ΔH) is formulated based on the liquid fraction (φ) and the latent heat of fusion (F) as follows:

$$\Delta H = \varphi F \tag{8}$$

In Eq. (9), the corresponding values of (φ) are given based on the temperature between the solidus temperature (T_s) and the liquidus temperature (T_l) [33].

$$\varphi = \begin{cases} 0 & if \quad T_{PCM} < T_s \\ \dfrac{T_{PCM} - T_s}{T_l - T_s} & if \quad T_s \le T_{PCM} \le T_l \\ 1 & if \quad T_{PCM} > T_l \end{cases} \tag{9}$$

The mathematical form of (S) introduced in Eq. (3) is described as follows:

$$S = -A(\varphi)V \tag{10}$$

The permeability function ($A(\varphi)$) controls the strength of momentum damping according to the expression below:

$$A(\varphi) = M_f \frac{(1 - \varphi)^2}{\varphi^3 + \varepsilon} \tag{11}$$

The mushy zone factor (M_f) and small numerical constant (ε) regulate the sharpness of the velocity suppression near the solid phase. In enthalpy-porosity simulations, the magnitude of (M_f) is critical in specifying the accuracy of the outcomes. Existing studies and modeling platforms have reported suitable values ranging from 10^4 to 10^8. Considering these guidelines, the present work utilizes $M_f = 10^6$ to ensure numerical stability and precision. The percentage improvement in melting performance of the hexagonal TSD compared to the reference configuration is evaluated using the melting enhancement ratio (E_m) [34].

$$E_m = \left[\frac{\varphi}{\varphi_{cc}} - 1\right] \times 100\% \tag{12}$$

where φ_{cc} is associated with the Core Case of TSD in which there are no inner hexagons and the bases.

4.2. Initial and boundary conditions

Initially, a homogeneous thermal field of 298.15 K is prescribed throughout the entire domain, including the PCM and all structural elements. The pressure inside the storage unit and in the ambient is set to 1 atm. The HTF tubes are maintained at a fixed boundary temperature of 333.15 K throughout the charging process. No-slip velocity and no-temperature-jump are imposed on all solid-fluid interfaces.

4.3. Computational approach and solver settings

The framework for modeling the introduced TSD is implemented using ANSYS Fluent. In this environment, the pressure-velocity coupling is handled using the SIMPLE algorithm, ensuring convergence of the incompressible flow field. A second-order upwind discretization is adopted for the convective terms to reduce numerical diffusion, while the PRESTO scheme is used for pressure interpolation to capture buoyancy-driven effects within the PCM accurately. Numerical stability is additionally improved by applying suitable under-relaxation techniques, with factors of (0.3) for pressure, (0.7) for momentum, (0.9) for the liquid fraction, and (1.0) for both density and energy. Moreover, the computations are advanced until the residual levels of the governing equations satisfy a tolerance of (10^{-6}).

5. System verification and numerical accuracy assessment

5.1. Quantitative validation against experimental temperature data

The reliability of the current simulation has been rigorously confirmed by comparing the results with the experimental work of Kousha et al. [35], who examined PCM melting characteristics in a multi-tube TSD. In that study, the surroundings were kept at 24 °C while the HTF entered the system at 80 °C. To achieve a reliable comparison, identical geometry and boundary conditions were reproduced in the present numerical simulation. More precisely, the configuration included three tubes enclosed within a cylindrical shell of 70 mm diameter, while each HTF tube had a diameter of 7.33 mm. Additionally, the HTF flow rate was set to 0.4 L/min, consistent with the experimental setup. The comparison between numerical and experimental results demonstrates a high level of agreement, both quantitatively and qualitatively. As shown in Fig. 2a, the predicted data closely match the experimental measurements, confirming the accuracy of the numerical model. This strong agreement confirms the reliability of the enthalpy-porosity formulation with $M_f = 10^6$ for predicting transient thermal

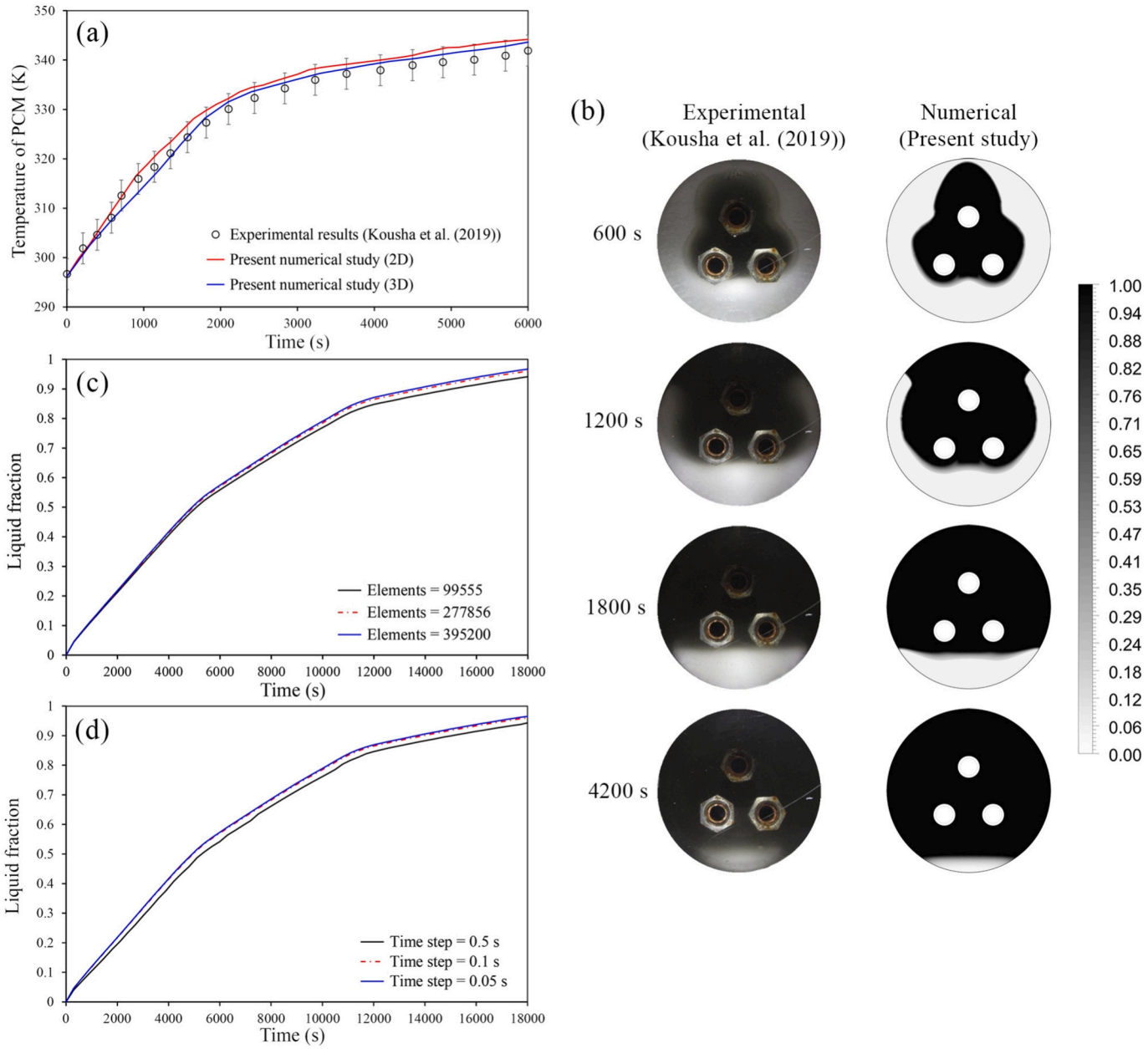

Fig. 2. Validation and numerical reliability of the present model: (a) comparison of predicted PCM temperature in 2D and 3D with experimental measurements; (b) qualitative charging pattern of PCM at selected times; (c) mesh independence analysis; (d) time-step sensitivity assessment.

behavior. In the present study, although the physical system has a finite length (800 mm) and is inherently three-dimensional, a 2D transient model was adopted to focus on the dominant heat transfer mechanisms in the radial direction, where the melting process primarily occurs. This simplification is based on the fact that the thermal gradients and phase change dynamics are significantly stronger across the cross-section than along the axial direction. As the HTF flows through the tubes, it gradually loses energy, which leads to a slight temperature reduction along the longitudinal direction. However, when the flow rate is sufficiently high, this temperature drop remains very small (typically below 0.5 K), making axial variations relatively weak compared to radial temperature differences. Therefore, neglecting axial effects is a reasonable assumption for capturing the main physics of the melting process while significantly reducing computational cost. To further justify this assumption, a 3D simulation was also performed for validation purposes, and the results are compared with the 2D model in Fig. 2a. As shown in this figure, both 2D and 3D numerical results follow very similar trends and show strong agreement with the experimental data. The 3D results are slightly lower than the 2D predictions, which is expected because the HTF temperature decreases gradually along the flow direction due to energy loss. This leads to a slightly reduced heat transfer rate and slower melting in the later stages in the 3D case. However, the deviation between the 2D and 3D results is relatively small, confirming that axial effects have a limited impact in the thermal behavior of the device. This is also consistent with findings reported in the literature, where axial variations are typically much smaller (about 2.5%) compared to radial changes [36]. It is also important to note that performing full 3D optimization would increase the computational cost significantly (approximately four times or more), making the optimization process much more time-consuming without a proportional gain in accuracy. Therefore, the 2D model provides a computationally efficient and sufficiently accurate framework for the purpose of this study, which is focused on geometry optimization and enhancement of energy absorption.

5.2. Qualitative validation of melting front evolution

Furthermore, the melting patterns presented in Fig. 2b show strong qualitative agreement, with similar phase front evolution and thermal behavior observed in both the simulation and the experiment. It should be noted that this work employs a 2D modeling framework, which inherently assumes no temperature variation in the longitudinal direction. In contrast, in the experimental setup, the temperature of the HTF decreases slightly as it flows downstream due to heat transfer, leading to minor longitudinal temperature gradients. As a result, the HTF temperature in the numerical model remains slightly higher than in the experiment. However, this difference is minimal and does not significantly affect the overall melting behavior or energy absorption trends. The melting evolution and phase change characteristics predicted in the present work closely follow those observed experimentally, confirming that the dominant heat transfer mechanisms are accurately captured. Therefore, based on the strong quantitative agreement and the consistent qualitative behavior, the developed numerical model can be considered valid and reliable for investigating the thermal performance of the proposed system. The validation performed in this study is intended to verify the numerical method and solution approach, rather than to directly validate the exact geometry proposed in the present work. The purpose of this validation is to demonstrate that the governing equations, numerical schemes, and phase change modeling approach are capable of accurately capturing the melting behavior of PCM systems under similar physical conditions. After confirming the reliability of the numerical framework, it is then applied to the proposed configuration, which differs geometrically but remains physically comparable. Therefore, the validation ensures the credibility of the simulation methodology, while the performance of the proposed geometry is evaluated through a comparative and parametric numerical investigation, rather than direct experimental validation.

5.3. Grid independence and mesh resolution selection

Fig. 2c demonstrates the impact of mesh density in the melt fraction evolution using quadrilateral grids. The coarsest mesh with 99,555 elements underestimates the liquid fraction compared to the finer meshes, particularly after 5000 s. This deviation indicates that the coarse grid is unable to fully resolve the buoyancy-driven convection and melt-front distortion occurring during active phase change. When the mesh density is increased to 277,856 elements, the predicted liquid fraction rises significantly and closely matches that obtained with the finest mesh. The curves corresponding to 277,856 and 395,200 elements are almost indistinguishable over the entire simulation time, with only negligible differences observed near the end of melting. As a result, the solution can be considered mesh independent at 277856 elements.

5.4. Time-step independence analysis

In PCM-based simulations, the choice of time step size plays an undeniable role in phase change dynamics. An excessively large time step may smooth rapid thermal transients, leading to numerical instability. In contrast, an overly small time step increases computational cost without providing meaningful improvements in accuracy. According to Fig. 2d, three different time-step sizes are applied to evaluate the convergence of the predicted melt fraction. The outcomes show that reducing the time step leads to progressively closer histories. It can be concluded that a time-step of 0.1 s was selected to ensure adequate temporal resolution for accurately tracking the transient evolution of the melting process while avoiding noticeable discretization effects.

6. Machine learning procedure

6.1. Artificial neural network (ANN)–based predictive model

ANNs have emerged as powerful data-driven tools for modeling complex, nonlinear relationships in thermal and energy systems [37]. Owing to their capability to learn from examples rather than relying on explicit governing equations, ANNs have been widely adopted as predictive models in energy storage research [38]. These models provide rapid, reliable estimates of system performance metrics once trained, thereby significantly reducing the computational burden of repeated high-fidelity numerical simulations [39]. Beyond mere prediction, predictive models play a strategic role in design optimization and parametric exploration. By establishing a functional mapping between design variables and performance indicators, ANNs enable fast sensitivity analysis and facilitate the integration of multi-objective optimization frameworks. Here, a predictive model utilizing an ANN has been created to predict the total stored thermal energy at two characteristic time instants: 9000 s and 18,000 s, corresponding to the intermediate and advanced stages of the PCM melting process, respectively. The ANN model is trained on a dataset generated from numerical simulations of the hexagonal TSD across a broad design space. The input layer of the ANN consists of three geometric parameters: the length of the first hexagon (*FL*), the length of the second hexagon (*SL*), and the inclination angle of the system (θ). As mentioned in Section 2, these parameters are not selected arbitrarily. Instead, they are carefully selected based on their dominant physical influence on heat transfer mechanisms. For instance, varying *SL* does not merely change the available heat transfer surface; it also directly determines the configuration of the tubes, including their distribution and coverage within the storage chamber. This dual influence makes *SL* a highly sensitive and governing parameter. Similarly, *FL* controls the internal conductive pathways, while θ affects buoyancy-driven convection. The additional geometric parameters, such as tube diameter, tube thickness, and wall thickness can also be investigated. However, these parameters were intentionally kept constant in the present study to ensure a controlled and consistent comparison across all configurations. The objective was to isolate the effect of the structural design itself rather than introduce multiple secondary variables that could obscure the primary physical insights. Moreover, the influence of these secondary parameters is relatively more predictable and less impactful compared to *FL*, *SL*, and θ. For example, increasing tube diameter or wall thickness generally leads to a straightforward increase in heat transfer area or conduction, whereas the selected parameters in this study simultaneously affect geometry, flow structure, and thermal pathways, making their role far more critical and nontrivial. For these reasons, the study focused on the most influential and design-defining parameters, while other geometric variables were excluded to maintain clarity and avoid unnecessary complexity.

As illustrated in Fig. 3a, the ANN predictive model is constructed using a systematic, iterative workflow to ensure robustness and predictive accuracy. Each step of this procedure is briefly outlined as follows:

* Loading data: The process starts by importing the dataset obtained from numerical simulations of the TSD. This dataset contains the input parameters (*FL*, *SL*, and θ) and forms the learning basis of the ANN model.
* Normalizing data: Before training, all input variables are normalized to a common numerical range. This step is essential to prevent parameters with larger magnitudes from dominating the learning process and to improve the network's numerical stability and convergence speed. Normalization also enhances the ANN's generalization when predicting unseen cases. Table 2 indicates the input parameters (*FL*, *SL*, and θ) of the ANN-based predictive model.

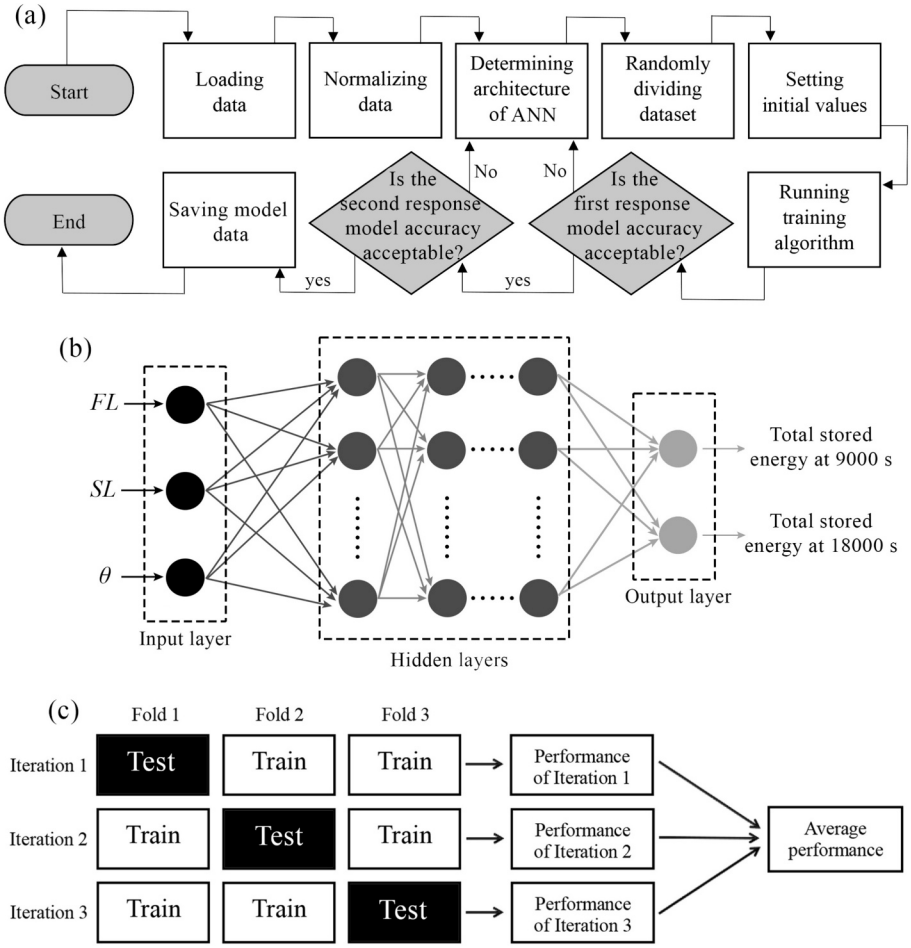

Fig. 3. (a) Flowchart illustrating the developing procedure and selecting the ANN-based predictive model. (b) Schematic architecture of the multilayer feedforward neural network with three inputs (FL, SL, and θ), multiple hidden layers, and two outputs representing the total stored energy at 9000 s and 18,000 s. (c) K-fold cross-validation procedure used to evaluate the performance of the ANN model.

Table 2
The input parameters (FL, SL, and θ) of the ANN-based predictive model.

Variable	Variable levels		
	-1	0	+1
FL (mm)	30	50	70
SL (mm)	100	130	160
θ (degree)	0	15	30

* Determining the ANN architecture: A multilayer feedforward neural network is constructed using MATLAB's feedforwardnet function. The number of hidden layers and neurons is selected through a trial-and-error procedure, aiming to achieve an optimal balance between model complexity and prediction accuracy. Within the hidden layers, a tanh-based transfer function is used to model the complex nonlinear correlations between the input parameters and the predicted outputs. The output layer utilizes the linear (purelin) activation function, which is suitable for continuous-valued regression problems such as total stored energy prediction.
* Randomly dividing the dataset: The complete dataset is randomly divided into three subsets. The model parameters are iteratively adjusted using the training dataset. In contrast, a separate validation dataset is used to assess predictive robustness and prevent overfitting during learning. The testing set is reserved for the final independent assessment of model accuracy.
* Setting initial values: The ANN's weights and biases are assigned randomly. This step is important because different initializations may lead the training algorithm toward different local minima. Consequently, multiple training runs can be performed to ensure the selected model is near-optimal.
* Running the training algorithm: Levenberg–Marquardt (LM) algorithm was used to train the ANN predictive model in this study. The choice of this algorithm is based on its well-established advantages in training feedforward neural networks, particularly for engineering applications with relatively moderate-sized datasets. The LM algorithm is a second-order optimization method that combines the benefits of the Gauss–Newton method and gradient descent. This hybrid nature enables it to achieve fast convergence while maintaining numerical stability, making it significantly more efficient than standard backpropagation methods for nonlinear regression problems. During training, the ANN iteratively adjusts its internal weights and biases to minimize the error between the anticipated and simulated values of the total stored energy at 9000 s and 18,000 s.
* Evaluating model accuracy and stopping criteria: After training, the ANN's predictive accuracy is evaluated for both response variables. If the accuracy of the first output (total stored energy at 9000 s) is not acceptable, the ANN architecture is modified, and the training process is repeated. Once the first response meets the predefined accuracy criteria, the second output (total stored energy at 18000 s) is assessed. If the accuracy of the second response is also unsatisfactory, the ANN architecture and training process are again revised. The

development process terminates when acceptable prediction accuracy is achieved simultaneously for both outputs on the validation and test datasets.

* Saving the trained model: The optimized ANN model, including its trained weights and biases, is saved for subsequent use. This trained predictive model is then coupled with the multi-objective optimization framework to specify optimal geometric configurations of the TSD rapidly.

Fig. 3b presents a schematic representation of the ANN architecture employed in this study. The network follows a multilayer feedforward structure. In the present study, the data are not randomly generated; they are obtained using a full factorial design of experiments (DoE) with three parameters (*FL*, *SL*, and θ), each at three levels. This method ensures that all combinations of parameter levels are systematically explored, including boundary and interaction effects. Therefore, the dataset is structured, comprehensive, and highly informative, rather than sparse or arbitrary. To further ensure that the model does not suffer from overfitting, a k-fold cross-validation technique was employed (illustrated in Fig. 3c), which is particularly suitable for limited datasets. As illustrated in Fig. 3c, the dataset is divided into multiple folds, and in each iteration, one fold is used for testing while the remaining folds are used for training. This process is repeated so that each subset of data is used once as a test set, and the overall efficiency of the final model is determined by taking the average of the outcomes from all iterations.

6.2. Genetic algorithm (GA)–based optimization

GA is a population-based stochastic optimization technique inspired by the principles of natural selection and evolutionary biology [40]. Unlike gradient-based methods, GAs do not require derivative information and are therefore particularly well suited for solving highly nonlinear, multimodal, and coupled optimization problems. Optimization plays a central role in configuration-oriented design of TSDs. The geometric parameters not only affect the heat transfer surface area but also regulate the internal flow structures and the evolution of the melting front within the PCM domain [41]. Consequently, systematic optimization is needed to fully exploit the potential of innovative geometries to ensure that the design achieves superior thermal performance compared to conventional configurations [42]. Here, the optimization procedure is conducted in two stages. Initially, single-objective optimization is applied to maximize two performance criteria independently:

* The total stored thermal energy at 9000 s
* The total stored thermal energy at 18000 s

These two objectives represent different charging stages of the thermal energy storage process. Conducting single-objective optimization for each target separately provides valuable insight into how the optimal geometric configuration may shift depending on whether fast energy absorption or long-term storage capacity is prioritized. Then, a multi-objective optimization framework is exerted to simultaneously enhance the total stored thermal energy at 9000 s and 18,000 s. This formulation captures the inherent trade-off between rapid charging performance and long-term energy storage capability. The outcome of this stage is a Pareto-optimal set of solutions, offering a spectrum of optimal design configurations that balance early-stage and late-stage energy storage performance. Such Pareto fronts provide designers with flexibility to select geometries based on specific operational priorities or application-driven requirements. For both the single-objective and multi-objective optimizations, the algorithm was configured with a population of 1000, an elite count of 50, a mutation probability of 0.01, a crossover probability of 0.8, and a maximum of 300 generations. In the present study, the stochastic uniform selection method was employed within the GA framework. In this approach, individuals are selected based on their fitness values using a probabilistic mechanism that ensures a balanced selection pressure across the population. Specifically, the method operates by mapping the cumulative normalized fitness of all individuals onto a line segment and then selecting parents at evenly spaced intervals along this line, starting from a randomly chosen point. This strategy ensures that individuals with higher fitness have a greater chance of being selected, while still allowing less-fit individuals to participate in the evolutionary process. The advantage of stochastic uniform selection lies in its ability to maintain population diversity while avoiding excessive bias toward only the best individuals. This helps prevent premature convergence and enhances the exploration capability of the GA, which is particularly important for solving complex, nonlinear optimization problems.

6.3. Multi-criteria decision-making using the TOPSIS method

The Technique for Order Preference by Similarity to Ideal Solution (TOPSIS) is a widely used multicriteria decision-making approach for ranking and selecting optimal alternatives in engineering design problems [43]. This method enables the simultaneous consideration of multiple performance indicators while accounting for their relative importance via weighting factors [14]. In this study, TOPSIS is employed to rank the non-dominated design solutions obtained from the multi-objective GA and to identify the most balanced optimal configuration. The detailed procedure of TOPSIS is mathematically expressed through Eqs. (13)–(19), which are explained as follows. Eq. (13) performs vector normalization of the decision matrix, where x_{ij} represents the value of the j^{th} criterion for the i^{th} alternative, and m is the number of alternatives. This step eliminates the influence of differences in units and scales across the criteria, enabling a fair comparison across all performance measures.

$$r_{ij} = \frac{x_{ij}}{\sqrt{\sum_{i=1}^{m} x_{ij}^2}} \tag{13}$$

In Eq. (14), each normalized criterion is multiplied by its corresponding weight w_j, reflecting the relative importance of each objective in the decision-making process. This step incorporates designer preferences or application-specific priorities into the evaluation.

$$v_{ij} = w_j \cdot r_{ij} \tag{14}$$

Eq. (15) defines the ideal solution for each criterion as the maximum weighted normalized performance across all alternatives.

$$x_j^{ideal} = \max\{v_{ij}\} \tag{15}$$

Eq. (16) depicts the anti-ideal solution as the minimum value of the weighted normalized criterion, representing the worst possible performance among the alternatives.

$$x_j^{anti-ideal} = \min\{v_{ij}\} \tag{16}$$

Eqs. (17) and (18) compute the Euclidean distance between each alternative and the ideal solution in the weighted normalized decision space. A smaller value of D_i^{ideal} denotes that the corresponding design is closer to the optimal performance.

$$D_i^{ideal} = \sqrt{\sum_{j=1}^{m} w_j \left(x_{ij} - x_j^{ideal}\right)^2} \tag{17}$$

$$D_i^{anti-ideal} = \sqrt{\sum_{j=1}^{m} w_j \left(x_{ij} - x_j^{anti-ideal}\right)^2} \tag{18}$$

Eq. (19) defines the closeness coefficient, which quantifies the relative proximity of each alternative to the ideal solution. Higher values of this coefficient indicate superior overall performance, as the alternative

is simultaneously closer to the ideal solution and farther from the anti-ideal solution. Based on the calculated closeness coefficients, the Pareto-optimal solutions are ranked, and the configuration with the highest closeness coefficient is selected as the final optimal design of the thermal energy storage system.

$$CC = \frac{D_i^{ideal}}{D_i^{ideal} + D_i^{anti-ideal}} \tag{19}$$

7. Results and discussion

7.1. Numerical simulation outcomes

In the present study, the primary objective is to enhance the energy storage capability of the system, which is the fundamental function of latent TSD. For this reason, the optimization process is based on total stored thermal energy at two representative times (9000 s and 18,000 s), corresponding to intermediate and near-complete charging stages. The selection of these two objectives is intentional and physically meaningful. When total stored energy is considered, it inherently reflects the combined effects of several important parameters, including latent heat absorption, sensible heat storage, melting progression, temperature distribution, PCM volume in the container, and effective heat transfer area. In other words, it serves as a comprehensive performance indicator that captures both the quantity and quality of thermal storage. In contrast, using isolated parameters such as liquid fraction or temperature alone may lead to incomplete or even misleading conclusions. For example, a configuration may exhibit a high liquid fraction while storing less total energy due to weaker sensible heat absorption. Similarly, temperature evolution alone cannot distinguish between latent and sensible energy contributions. Therefore, optimizing based solely on such parameters does not fully represent the actual storage performance. Other criteria, such as charging rate, melting completion time, temperature uniformity, and material usage are also important in real engineering applications. In this work, these aspects are not ignored, but rather analyzed separately through detailed transient plots, including liquid fraction evolution, temperature fields, and energy components. However, they are not directly included as optimization objectives in order to maintain a focused and computationally efficient optimization framework.

A comprehensive parametric investigation was conducted to assess the effects of geometric configuration and system orientation on thermal energy storage performance during the PCM melting process. Specifically, the influence of the first hexagon length (*FL*), the second hexagon length (*SL*), and the inclination angle of the system (θ) was investigated. Based on the controlled variation of these three parameters, 27 distinct design cases were developed and numerically simulated. These cases represent all meaningful combinations of the selected parameter levels and were deliberately constructed to capture the coupled effects of conductive heat transfer enhancement and buoyancy-driven natural convection within the molten PCM. The simulations were conducted using the same boundary and operating conditions to ensure a fair and consistent comparison among all configurations. To clearly quantify the performance improvement achieved by the proposed multi-hexagonal architecture, the results from 27 parametric cases are compared with a core case configuration. The core case represents a conventional shell-and-tube-like design consisting solely of the outer hexagonal shell and six embedded HTF tubes, without the internal hexagonal frameworks or the connecting bases. This reference case serves as a baseline to isolate the contribution of the internal bases and concentric hexagonal segmentation to heat transfer enhancement and energy storage capacity. Table 3 summarizes the numerical results for the 27 parametric configurations, along with those for the core case configuration. For each case, the table reports the liquid fraction and the total stored thermal energy at two representative time instants, namely 9000 s (2.5 h) and 18,000 s (5 h). Two different time instants were deliberately selected to cover the entire melting process, including both the intermediate stage (9000 s), where melting is still progressing, and heat transfer mechanisms are highly transient, and the final stage (18,000 s), where the system approaches or reaches complete melting. Reporting data at both times enables a comprehensive assessment of melting acceleration and

Table 3
Numerical results of liquid fraction and total stored energy for the 27 parametric cases and the core case at 9000 s and 18,000 s.

Case number	Variables			Liquid fraction at different times		Total stored energy at different times (kJ)	
	FL (mm)	*SL* (mm)	θ (degree)	9000 s (2.5 h)	18,000 s (5 h)	9000 s (2.5 h)	18,000 s (5 h)
1	30	100	0	0.735	0.961	10,265	12,994
2	30	160	0	0.822	1	11,148	13,470
3	30	100	30	0.737	0.964	10,287	13,063
4	30	130	0	0.925	1	12,355	13,537
5	30	100	15	0.732	0.963	10,232	13,027
6	30	130	15	0.923	1	12,330	13,537
7	30	130	30	0.918	1	12,288	13,537
8	30	160	15	0.823	1	11,165	13,468
9	30	160	30	0.825	1	11,184	13,469
10	50	130	15	0.917	1	12,272	13,537
11	50	130	0	0.920	1	12,304	13,537
12	50	160	0	0.820	1	11,125	13,469
13	50	100	15	0.732	0.963	10,229	13,024
14	50	100	30	0.735	0.964	10,261	13,059
15	50	100	0	0.734	0.960	10,245	12,984
16	50	130	30	0.913	1	12,237	13,537
17	50	160	15	0.822	1	11,150	13,467
18	50	160	30	0.826	1	11,183	13,466
19	70	160	30	0.827	0.992	11,203	13,272
20	70	100	0	0.716	0.961	9987	12,995
21	70	130	30	0.882	1	11,936	13,532
22	70	130	15	0.877	1	11,879	13,532
23	70	100	30	0.717	0.965	10,011	13,070
24	70	100	15	0.717	0.964	10,000	13,040
25	70	160	0	0.823	0.994	11,168	13,277
26	70	130	0	0.881	1	11,914	13,532
27	70	160	15	0.824	0.993	11,171	13,280
Core Case	–	–	–	0.262	0.505	4481	7621

ultimate energy storage capability.

At 9000 s, the liquid fraction for the proposed cases ranges from approximately 0.70 to 0.93, depending on the geometric configuration and inclination angle. In stark contrast, the core case exhibits a liquid fraction of only 0.262. This corresponds to an enhancement of approximately 167–244% in the liquid fraction for the proposed cases compared to the core case, clearly demonstrating the effectiveness of the internal hexagonal bases and segmentation in accelerating PCM melting during the early and intermediate stages. By 18,000 s, 15 cases achieved complete melting (liquid fraction = 1), while the remaining configurations reached liquid fractions of 0.96–0.99, indicating near-complete melting. Conversely, the core case attains a liquid fraction of only 0.505, confirming that nearly half of the PCM remains solid even after 5 h of heating. This highlights the substantial limitation of the conventional shell-and-tube-like configuration in promoting heat penetration into the PCM core. The total stored energy results exhibit a comparable trend. At 9000 s, the lowest stored energy among the proposed configurations is 9987 kJ for Case 20, while the highest is 12,355 kJ for Case 4. In comparison, the core case stores only 4481 kJ at the same time. This translates to an energy storage enhancement of approximately 123% for Case 20 and 176% for Case 4 relative to the core case, even during the intermediate melting stage. At 18000 s, the minimum stored energy among the proposed cases is observed for Case 15, with 12,984 kJ, whereas the maximum value of 13,537 kJ is achieved by multiple cases that reach complete melting. In contrast, the core case stores only 7621 kJ after 5 h. Accordingly, the configurations that reach full melting exhibit an energy storage improvement of approximately 78% over the core case, while even the least-performing case at this time (Case 15) shows an enhancement of about 70%.

From the total set of 27 numerically simulated configurations, a

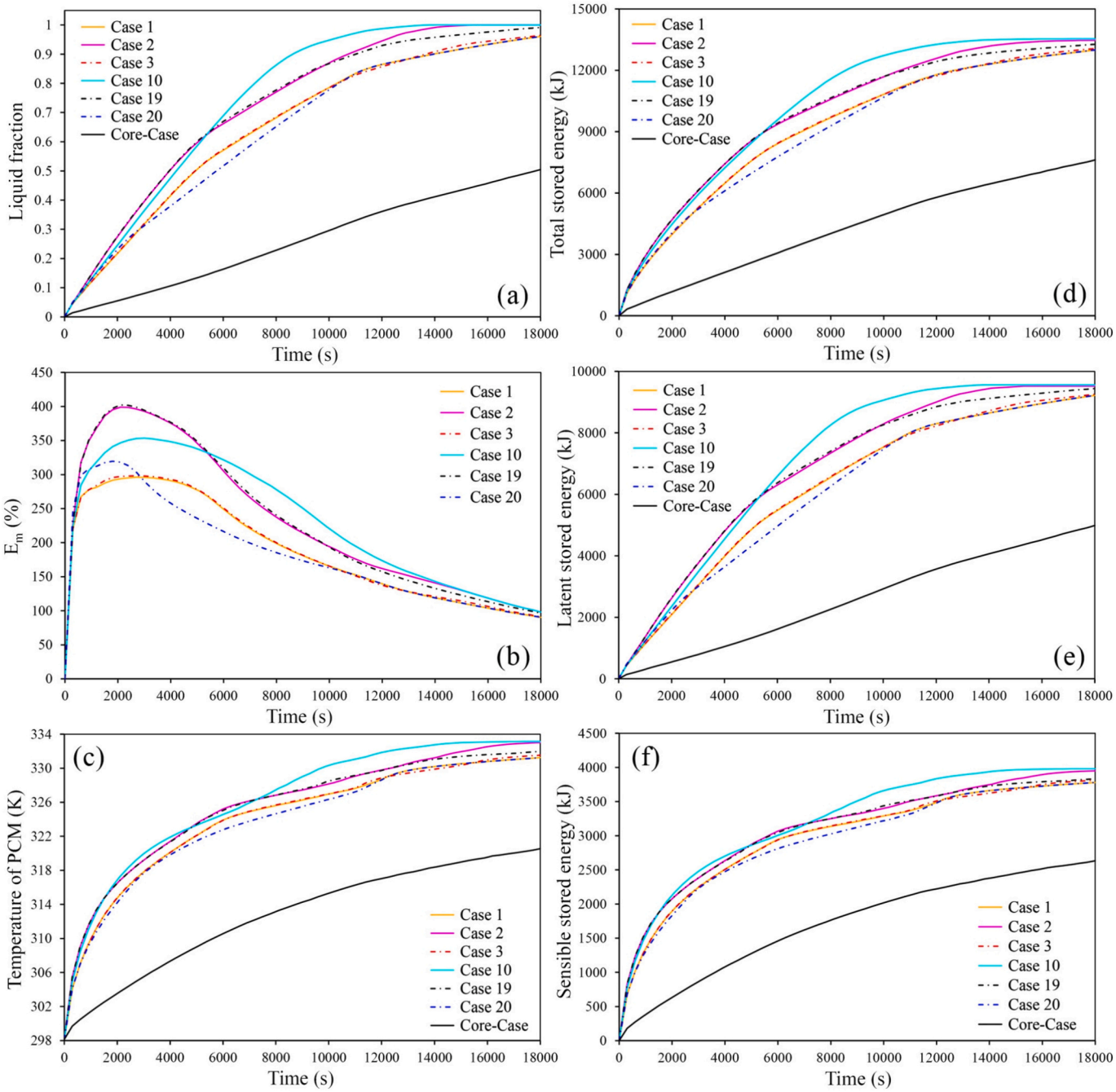

Fig. 4. Time-dependent melting performance indicators for selected configurations compared with the core case.

subset of representative cases is selected in Fig. 4 to provide a clearer, more detailed interpretation of the impacts of hexagon length and system inclination angle on the charging behavior and thermal performance of the proposed TSD. These cases were deliberately chosen to span the full design space, including extreme, intermediate, and asymmetric geometric configurations, thereby enabling a meaningful physical interpretation of the observed trends. Specifically, Case 1 represents a configuration with the shortest hexagon lengths and the lowest system inclination angle. Case 19 corresponds to the opposite extreme, featuring the longest lengths of both hexagons combined with the highest inclination angle. Intermediate values of both hexagon lengths and the inclination angle characterize case 10. The shortest first hexagon length, the longest second hexagon length, and the lowest inclination angle define case 2. Case 3 combines the shortest hexagon lengths with the highest inclination angle. Finally, Case 20 represents a configuration with the longest first hexagon length, the shortest second hexagon length, and the lowest inclination angle.

As shown in Fig. 4a, the liquid fraction in all selected configurations is consistently higher than that of the core case throughout the entire melting process, confirming the substantial enhancement achieved by the internal hexagonal frameworks and bases. Moreover, the noticeable differences in the liquid fraction curves across the selected cases demonstrate that the configurations are not only distinct but also effectively capture the system's sensitivity to geometric and inclination variations. Among the proposed designs, Case 10 initially exhibits a relatively slower increase in liquid fraction, but subsequently completes the melting process rapidly with a nearly uniform slope. In contrast, several other configurations display a faster initial melting rate followed by a pronounced reduction in slope. A representative example is Case 19, which incorporates the longest lengths of both the first and second hexagons. As the hexagon lengths increase, the internal frameworks expand and move closer to the outer shell (third hexagon, as illustrated in Fig. 1b). Consequently, the three hexagonal structures approach each other, leading to a high concentration of heat transfer surface areas in localized regions of the system. This geometric convergence promotes rapid heat distribution from the HTF tubes to nearby conductive surfaces. However, the PCM volume enclosed between these closely spaced surfaces is relatively small, leading to rapid melting in those regions. At the same time, the central regions of the storage domain, which are comparatively deficient in heat transfer surfaces, rely primarily on natural convection and conduction for heat transport. Heat penetration into these zones is therefore time-consuming, ultimately leading to a reduction in the slope of the melting rate at later stages. A similar melting behavior is observed in Case 2, where the maximum second-hexagon length strongly influences HTF tube placement and results in non-uniform heat distribution. Overall, Case 10 emerges as the most effective configuration. In Case 10, all three geometric parameters are set at their mid-range values ($FL = 50$ mm, $SL = 130$ mm, and $\theta = 15^{\circ}$), which creates a balanced configuration from a thermal perspective. The intermediate value of SL positions the HTF tubes neither near the center nor adjacent to the outer walls. Instead, they are located in a thermally optimal intermediate region, allowing effective heat distribution toward both the core and peripheral PCM zones. This enhances conductive heat spreading throughout the domain. At the same time, the inclination angle of 15° promotes natural convection without causing excessive stratification. When $\theta = 0^{\circ}$, the vertical distance between the hexagonal layers is minimized, limiting buoyancy-driven flow and weakening the thermosyphon effect. By increasing the angle to 15°, the effective vertical height of the PCM domain increases, enabling stronger buoyancy-induced circulation and improved mixing of molten PCM. This leads to a more efficient combination of conduction and natural convection. Therefore, Case 10 performs best because it achieves a balanced interaction between conductive heat transfer (via optimal tube placement) and enhanced natural convection (via moderate inclination), resulting in improved overall thermal performance. In contrast, Case 20 exhibits the weakest performance among the selected designs. In this case, the combination of a large FL and a short SL reduces the distance between the two inner hexagons, resulting in an ineffective distribution of conductive pathways and diminished overall melting performance.

Fig. 4b illustrates the melting enhancement ratio (E_m), which quantitatively compares the melting performance of each proposed configuration with that of the core case at any given time. Positive values of E_m throughout the entire melting process confirm that all selected configurations outperform the core case, demonstrating the effectiveness of the internal hexagonal frameworks and bases in accelerating PCM melting. Consistent with the liquid fraction trends observed in Fig. 4a, Cases 19 and 2 exhibit the highest E_m values during the early stages of melting, indicating rapid initial enhancement. Specifically, Case 19 reaches a peak melting enhancement ratio of 402% at approximately 2100 s, indicating that its melting performance is more than four times greater than that of the core case at that time. Also, Case 10 attains an E_m value of 353% at around 3050 s, reflecting strong and sustained melting enhancement. Two key observations can be drawn from Fig. 4b. First, all E_m curves gradually converge at later times, indicating that the melting processes across all configurations approach completion. Second, the slopes of all E_m curves decrease progressively with time. This behavior arises because, while most of the proposed configurations complete or nearly complete melting at advanced times, the core case continues to melt at a slower rate. Hence, the relative performance gap between the proposed designs and the core case decreases, resulting in a lower melting enhancement ratio.

Based on Fig. 4c, of the chosen cases, Case 10 shows the fastest temperature increase, reaching higher PCM temperatures (approximately 333.15 K) earlier than the other cases. This behavior is due to the more even spatial distribution of heat-transfer surfaces in Case 10, which facilitates effective heat conduction from the HTF tubes to the bases and the three hexagonal frames while simultaneously supporting buoyancy-driven convection. In contrast, the core case, which consists solely of HTF tubes and the outer shell and lacks internal hexagonal frameworks and bases, exhibits significantly lower temperature levels, with the PCM temperature rising only to approximately 320.54 K. This limitation arises because heat transfer in the core case is predominantly localized near the HTF tubes. The absence of internal conductive pathways restricts heat penetration into the central PCM regions, leading to large temperature gradients and inefficient use of the storage volume. Consequently, a significant part of the PCM stays at lower temperatures, which reduces the average PCM temperature and delaying the onset of melting. A distinct plateau region is also evident in Fig. 4c, particularly between 6000 and 12,000 s. This region corresponds to the phase change interval, during which most of the supplied thermal energy is absorbed as latent heat of fusion, rather than causing a significant rise in temperature. During this stage, the PCM temperature remains nearly constant while melting progresses internally. The plateau is not represented as a perfectly flat line in Fig. 4c because the reported values correspond to the averaged PCM temperature. In reality, different PCM regions undergo phase change at slightly different times due to spatial variations in heat transfer. If the local PCM temperature at individual spatial points were reported instead of the average value, the plateau region would appear much more distinctly as a flat temperature interval.

In Fig. 4d, Case 19 exhibits the highest energy storage rate at the early stages of melting, attributed to its large hexagonal dimensions and elevated inclination angle, which intensify initial heat transfer from the HTF to the PCM. However, as time progresses, Case 10 surpasses Case 19 regarding stored energy, a pattern that aligns completely with the higher liquid fraction of Case 10 observed in Fig. 4a and its higher average PCM temperature shown in Fig. 4c. By 18,000 s, Case 10 completes its melting process and reaches a total stored energy of 13,537 kJ, which represents the maximum energy storage among the examined configurations. In contrast, Case 19 stores 13,272 kJ, despite its strong initial performance, indicating that its geometric configuration limits complete and uniform heat utilization at later stages. The core case, by comparison, stores only 7621 kJ after 18,000 s, highlighting the substantial enhancement

achieved by incorporating the internal hexagonal frameworks and bases. An important observation from Fig. 4d is that Case 10 attains its maximum energy storage within approximately 14,000 s, after which the stored energy curve flattens. This behavior indicates that the PCM has fully melted and absorbed the available thermal energy within a shorter charging duration. Such a feature is particularly advantageous for practical TSD applications, as it suggests that the storage capacity can be further increased by arranging two hexagonal containers in series, thereby accommodating a larger PCM volume while maintaining efficient charging performance.

Fig. 4e and f further decompose the total stored energy into its latent and sensible components, respectively, providing deeper insight into the underlying energy storage mechanisms. As shown in Fig. 4e, latent energy storage dominates the charging process across all proposed configurations, reflecting the effective utilization of the PCM's phase-change capacity. Case 10 again demonstrates superior performance, achieving higher latent energy storage at a faster rate, which confirms its ability to promote uniform melting throughout the storage domain. In contrast, the core case exhibits a significantly slower increase in latent energy, indicating delayed and incomplete melting due to insufficient internal heat-transfer pathways. This deficiency is consistent with the lower liquid fraction and PCM temperature trends previously discussed. Fig. 4f presents the evolution of sensible energy storage, which follows a similar trend but with lower absolute magnitudes compared to latent energy. The proposed configurations, particularly Case 10, store sensible energy more rapidly than the core case due to enhanced conductive and convective heat transfer. However, once the PCM temperature approaches equilibrium, the growth of sensible energy diminishes, and latent heat storage becomes the dominant mechanism.

7.2. Performance evaluation of the ANN-based predictive model

Following the extraction of performance indicators from numerical simulations, these results were used as benchmark data to develop and validate the ANN-based predictive model. The numerical outcomes for the total stored energy at half charging time (*SEH*) and full charging time (*SEF*) served as the supervised learning targets for the network. During the development of the ANN structure, various configurations were tested, including different numbers of hidden layers and neurons. It was found that increasing the number of hidden layers did not significantly improve prediction accuracy; instead, it introduced additional computational complexity and led to weaker convergence behavior. Therefore, a single hidden layer was selected as the optimal architecture. This result indicates that the nonlinear relationship between the input parameters (*FL*, *SL*, and θ) and the thermal responses (*SEH* and *SEF*) can be effectively captured without introducing unnecessary structural complexity. After selecting the single hidden-layer configuration, the number of neurons in this layer was varied from 2 to 8. The purpose of this parametric investigation was to identify the optimal balance between underfitting (insufficient neurons) and overfitting (excessive neurons). Increasing the number of neurons beyond a certain limit improved the accuracy for the training data but reduced the accuracy for validation and test datasets. This behavior is a clear indication of overfitting. The results demonstrated that a 3–6–2 architecture achieves the highest prediction accuracy for both responses simultaneously.

Table 4 depicts the optimized weights and biases of the selected 3–6–2 ANN model. The hidden layer consists of six neurons, each connected to the three input parameters through corresponding weight coefficients. The weight matrix (6 × 3) defines the strength and direction of influence of *FL*, *SL*, and θ on each hidden neuron. Positive weights illustrate a direct correlation, while negative values imply an inverse relationship within the learned nonlinear mapping. The hidden layer biases (6 × 1) serve as adjustable thresholds, adjusting each neuron's activation and enhancing the model's flexibility in capturing nonlinear behavior. These biases play a critical role in accurately representing the complex interactions between geometric configuration and heat-absorption mechanisms. The output layer contains two independent sets of weight vectors and biases, corresponding to *SEH* and *SEF* models. Each output neuron receives contributions from all six hidden neurons (6 × 1). The associated scalar bias term further adjusts the final predicted value. The separation of output parameters ensures that the ANN can independently learn the distinct temporal behaviors governing intermediate and full charging stages.

Table 5 evaluates the ANN model's predictive accuracy using two standard statistical performance metrics: the coefficient of determination (R^2) and the root mean square error (RMSE).

$$R^2 = 1 - \frac{\sum_{i=1}^{m} \left(r_{num} - r_{pred}\right)^2}{\sum_{i=1}^{m} \left(r_{num} - \overline{r_{pred}}\right)^2} \tag{20}$$

$$RMSE = \sqrt{\frac{\sum_{i=1}^{m} \left(r_{pred} - r_{num}\right)^2}{m}} \tag{21}$$

The R^2 values for both *SEH* and *SEF* are equal to 0.999, indicating an almost perfect correlation between the ANN predictions and the numerical simulation data. This extremely high value confirms that the network successfully captures the nonlinear mapping between geometric design variables and thermal energy storage performance. The RMSE values further quantify the average deviation of the predictions. For *SEH*, the RMSE is 20.887, while for *SEF* it is 6.893. These relatively small error magnitudes, compared to the overall scale of stored energy values, demonstrate the model's high precision. The lower RMSE observed for *SEF* suggests that the ANN captures the near-saturated charging behavior with slightly higher stability than the transient mid-time response. The simultaneous achievement of very high R^2 and low RMSE values confirms that the selected 3–6–2 ANN architecture provides strong predictive capability within the investigated design space and parameter ranges. In other words, the model can reliably predict the thermal performance of configurations that fall within the bounds of the training dataset and can therefore be confidently used for optimization within those limits. Therefore, the trained ANN model is considered sufficiently accurate to be integrated with the GA optimization framework. In the present study, the dataset consists of 27 numerical cases generated using a full factorial design of experiments. Following the

Table 4
Optimized weights and biases of the selected 3–6–2 ANN model for predicting SEH (stored energy at half charging time) and SEF (stored energy at full charging time).

Hidden layer				Output layer			
Weights (6 × 3)			Biases (6 × 1)	Model of *SEH*		Model of *SEF*	
				Weights^T (6 × 1)	Bias (1 × 1)	Weights^T (6 × 1)	Bias (1 × 1)
3.877	−0.603	0.109	−1.470	−0.137	−1.090	0.025	−1.316
1.179	1.271	0.015	−2.433	−0.341		−0.992	
1.165	−4.441	0.057	3.811	0.632		0.048	
0.369	−2.207	−2.095	−2.383	0.076		−0.037	
−0.019	−3.160	−0.104	−2.570	−1.142		−1.226	
−2.078	2.403	0.039	−2.752	0.156		−0.097	

Table 5
Statistical performance indicators of the ANN predictive model for SEH and SEF predictions.

Loss function	ANN model							
	SEH				*SEF*			
	Total	Train	Validation	Test	Total	Train	Validation	Test
R^2	0.9994	0.9999	0.9983	0.9915	0.9990	0.9995	0.9965	0.9737
RMSE	20.887	6.052	31.863	41.898	6.893	4.974	12.438	6.9642

ANN development procedure, 70% of the data (19 cases) were used for training the network, while the remaining 30% (8 cases) were reserved for independent validation and testing. Specifically, 4 cases were used for validation and 4 cases were used for testing. Consequently, a substantial portion of the dataset was not directly involved in the weight adjustment process, allowing the predictive capability of the network to be evaluated on unseen data. Furthermore, the dataset partitioning was performed using a random allocation procedure, which is the standard approach employed by MATLAB's neural network toolbox. This random distribution ensures that the training, validation, and testing subsets contain representative samples from the entire dataset and minimizes the possibility of bias associated with a fixed partitioning strategy. The predictive performance on this unseen data was carefully evaluated, and the corresponding error metrics (loss functions) are given in Table 5,

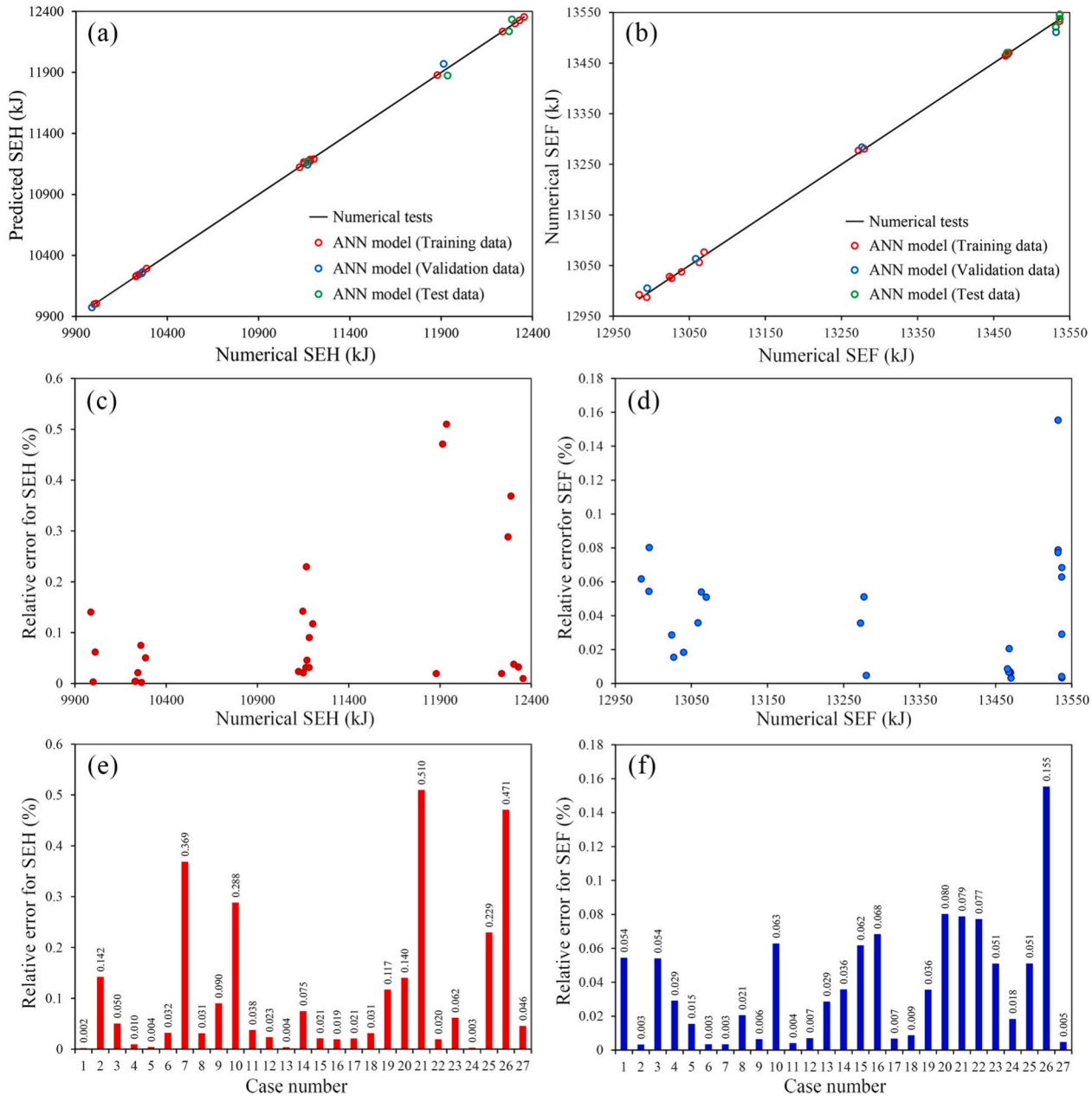

Fig. 5. Performance evaluation of the ANN predictive model: (a) predicted vs. numerical SEH, (b) predicted vs. numerical SEF, (c) relative error of SEH vs. response values, (d) relative error of SEF vs. response values, (e) relative error of SEH vs. case number, and (f) relative error of SEF vs. case number.

providing additional confirmation of the robustness of the model. Table 5 clearly demonstrates that the developed ANN-based predictive model is capable of accurately estimating both the training data and the unseen data (validation and test sets).

Fig. 5a and b present a direct comparison between the ANN-predicted values and the corresponding numerical results for both stored energy at half-charging time (*SEH*) and final stored energy (*SEF*). In these figures, the training, validation, and test data are all plotted together. It is evident that nearly all data points lie very close to the diagonal line representing perfect agreement. This indicates that the ANN model has successfully captured the underlying relationship between the input parameters (*FL*, *SL*, and θ) and the output responses. Importantly, the validation and test data, which were not used during training, also follow the same trend with high accuracy, confirming that the model does not suffer from overfitting and performs reliably for unseen cases. Fig. 5c–f further quantify the prediction performance by presenting the relative errors for both *SEH* and *SEF*. Fig. 5c and d illustrate the relative error as a function of the response values, showing how prediction accuracy varies across different energy levels. Meanwhile, Fig. 5e and f display the relative error for each individual case number, providing a clearer case-by-case evaluation. In all these plots, the prediction errors remain consistently low. As can be observed, the relative error for both responses is below 0.5% in all cases, which confirms the excellent predictive capability of the developed ANN model. Besides, the results of the k-fold cross-validation showed that R^2 values consistently remained above 98% for all folds, indicating that the model predictions are stable and not sensitive to how the data are partitioned.

Fig. 6a–f are 3D response surface plots generated from the trained ANN model. These plots illustrate the combined effects of two design variables at a time on the performance indices (*SEH* and *SEF*), with the third parameter implicitly accounted for in the trained model. The color gradient represents increasing performance values. Based on Fig. 6a, increasing *SL* initially increases *SEH*, after which *SEH* begins to decrease. This non-monotonic behavior is consistent across different *FL* values, indicating that the optimal *SL* range is relatively independent of *FL*. Increasing *FL* generally decreases *SEH*. The initial increase in *SEH* with *SL* can be attributed to improved heat transfer and enhanced energy storage capacity. However, beyond an optimal *SL* value, further increases may reduce thermal interaction efficiency or alter flow distribution unfavorably, leading to decreased stored energy. In Fig. 6b, the color variation range is noticeably smaller compared to Fig. 6a. This indicates that *FL* and θ have a less significant impact on *SEH* (at half charging time) compared to *SL*. This suggests that *SL* is the dominant parameter influencing stored energy. Physically, this is reasonable because: (1) *SL* directly affects the heat transfer surface area. (2) *SL* influences the configuration and arrangement of the HTF tubes, which strongly impacts thermal distribution and energy absorption efficiency. Fig. 6c further confirms the dominant role of *SL*. Similar to Fig. 6a, increasing *SL* initially increases *SEH*, followed by a decrease beyond an optimal value. This behavior is consistent across different θ values, showing that the trend is largely independent of θ. The lower row presents the corresponding ANN-predicted response surfaces for *SEF*. From these plots, increasing *SL* initially increases *SEF*, then causes a very slight decrease, suggesting an optimal *SL* value for energy storage efficiency. Increasing θ increases *SEF* to some extent, suggesting that inclination angle positively contributes to energy fraction. Increasing *FL* decreases *SEF*, consistent with its negative influence observed in the *SEH* results. Overall, Fig. 6a–f demonstrate that *SL* is the most influential design parameter affecting both *SEH* and *SEF*. It exhibits a clear optimal range, while *FL* generally has a negative effect and θ has a moderate positive influence (particularly on *SEF*). These response surfaces provide valuable insight for geometric optimization of the system.

7.3. GA-based optimization of design parameters

Although response surface plots provide valuable insight into the interactions among design variables and their qualitative influence on *SEH* and *SEF*, they are not sufficient for making accurate, precise design decisions. The response surfaces help identify general trends and approximate optimal regions; however, determining the exact

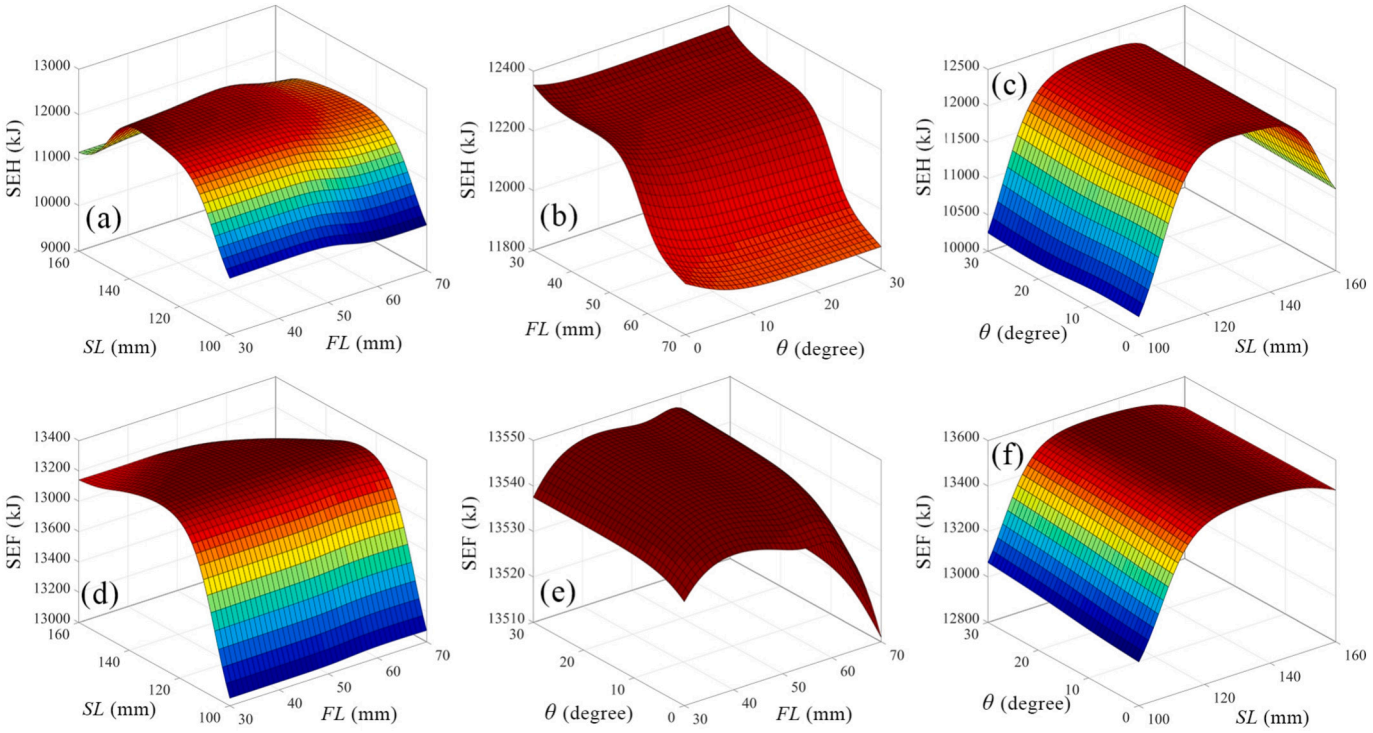

Fig. 6. ANN-predicted response surfaces illustrating the effects of structural parameters (*SL*, *FL*, and θ) on *SEH* and *SEF*. Panels (a)–(c) present *SEH* variations with paired parameters, while panels (d)–(f) show the corresponding *SEF* response surfaces.

combination of variables that maximizes system performance requires a robust optimization technique. Therefore, a highly accurate optimization method is necessary. In the present study, a GA is employed to determine the optimal design parameters. The selection of the GA in this study is primarily motivated by the nature of the optimization problem. The relationship between the design variables (*FL*, *SL*, and θ) and the objective functions (*SEH* and *SEF*) is highly nonlinear, coupled, and potentially multimodal, as it is governed by complex interactions between conduction, natural convection, and phase change phenomena. In such cases, classical gradient-based optimization methods such as fmincon may not be suitable, as they rely on smoothness and gradient information and are prone to being trapped in local optima, especially when the design space contains multiple peaks. In contrast, GA is a global, population-based optimization technique that does not require gradient information and is highly effective in exploring complex search spaces. Its stochastic nature allows it to avoid premature convergence and increases the likelihood of identifying global or near-global optimal solutions. This makes GA particularly appropriate for coupling with ANN-based surrogate models, where the objective functions may not have explicit analytical forms. Compared to random search, although simple to implement, it is generally inefficient and lacks guided exploration of the design space. It requires a significantly larger number of function evaluations to achieve results comparable to GA, especially in multi-objective problems. In contrast, GA employs selection, crossover, and mutation mechanisms to iteratively improve the population, leading to faster convergence toward optimal regions. Additionally, a key objective of this study is to perform multi-objective optimization and obtain a Pareto front of optimal solutions. GA-based approaches are inherently well-suited for this purpose, as they can simultaneously handle multiple conflicting objectives and generate a diverse set of non-dominated solutions in a single run. Methods like fmincon are not naturally designed for multi-objective optimization without significant modifications.

Owing to the strong predictive accuracy of the trained ANN model, it is coupled with GA to evaluate candidate solutions during the optimization process rapidly. Initially, single-objective optimization is performed. The optimization process is conducted separately for two performance criteria:

* The total stored thermal energy at 9000 s (*SEH*)
* The total stored thermal energy at 18000 s (*SEF*)

Table 6 presents the optimal design variables obtained from the GA-based single-objective optimization. Two distinct optimal cases are identified:

* Optimal Case 1 (*OpC1*) corresponds to the maximization of *SHE*
* Optimal Case 2 (*OpC2*) corresponds to the maximization of *SEF*

For *OpC1*, the optimal configuration is achieved at: $FL = 30$ mm, $SL = 137.140$ mm, and $\theta = 30°$. This result indicates that maximizing stored energy at 9000 s favors the minimum *FL* value within the design range and a relatively high *SL* value, while the inclination angle reaches its upper bound. For *OpC2*, the optimal design variables are: $FL = 58.760$ mm, $SL = 128.140$ mm, and $\theta = 30°$. In this case, maximizing stored energy at 18000 s requires a moderate *FL* value and a slightly lower *SL* compared to *OpC1*, while θ again reaches its maximum allowable value.

Table 6
Optimal design variables obtained from single-objective GA optimization for maximizing SEH and SEF.

Optimized response	Design symbol	Design variables		
		FL (mm)	*SL* (mm)	θ (degree)
SEH	*OpC1*	30	137.140	30
SEF	*OpC2*	58.760	128.140	30

However, in practical engineering applications, treating performance objectives independently is rarely realistic. Short-term and long-term energy storage requirements are inherently coupled and optimizing one objective at the expense of the other may lead to suboptimal system behavior. Therefore, multi-objective optimization is required to simultaneously consider both *SEH* and *SEF* and identify a balanced compromise solution. The outcomes of the multi-objective GA optimization are illustrated in Fig. 7, which presents the distribution of random solutions, the extracted Pareto-optimal front, and the final design selected using a decision-making technique. Fig. 7 shows the trade-off relationship between *SEH* and *SEF* obtained from the ANN–GA framework. As expected, the Pareto front clearly illustrates the trade-off between *SEH* and *SEF*. To select a single, practically optimal design from the Pareto front, TOPSIS is applied. This technique identifies the solution that simultaneously minimizes the distance from the ideal solution and maximizes the distance from the non-ideal solution. The TOPSIS-selected design owns a closeness coefficient of 0.872, suggesting a significant balance between the two competing objectives. The optimal compromise design selected by TOPSIS, referred to as Optimal Case 3 (*OpC3*), corresponds to $FL = 30$ mm, $SL = 135.549$ mm, and $\theta = 30°$. As shown in Fig. 7, the performance of *OpC3* lies between those of *OpC1* and *OpC2* and is notably closer to *OpC1*. This proximity reflects the strong influence of early-stage heat transfer enhancement on overall system performance, while still maintaining excellent long-term energy storage capability.

Table 7 presents a detailed validation by evaluating the optimization findings against the values acquired by the ANN with the corresponding numerical simulation results for the three optimized cases: *OpC1* (*SEH* maximization), *OpC2* (*SEF* maximization), and *OpC3* (multi-objective compromise solution). For *OpC1*, the predicted *SEH* and *SEF* values are 12,386 kJ and 13,525 kJ, respectively, while the numerical results are 12,387 kJ and 13,526 kJ. The associated errors are extremely small (0.009% for *SEH* and 0.007% for *SEF*), demonstrating nearly perfect agreement between the ANN model and numerical simulations. For *OpC2*, the predicted *SEH* and *SEF* are 12,019 kJ and 13,548 kJ, compared with numerical values of 12,085 kJ and 13,539 kJ. Although the *SEH* error (0.546%) is slightly higher than in the other cases, it remains well below 1%, and the *SEF* error is only 0.066%. This still confirms excellent predictive capability. For *OpC3*, which represents the compromise solution obtained from TOPSIS, the predicted *SEH* and *SEF* values (12,384 kJ and 13,529 kJ) are again in outstanding agreement with the numerical results (12,382 kJ and 13,528 kJ), with very small errors of 0.008% and 0.007%, respectively. Overall, the very low error percentages reported in Table 7 clearly depict the superior accuracy of the ANN-based predictive model in anticipating both performance criteria (*SHE* and *SEF*).

Fig. 8a illustrates the liquid fraction for the three optimized configurations (*OpC1*, *OpC2*, and *OpC3*) compared with the core case. The three optimized designs exhibit very similar melting trends, characterized by a steep increase in liquid fraction during the early charging stage, followed by a gradual approach toward complete melting. At 2.5 h (9000 s), *OpC1* reaches a liquid fraction of 0.928, *OpC2* reaches 0.896, and *OpC3* reaches 0.930. This indicates that more than 89% of the PCM has already melted in all optimized configurations at mid-charging time. Among them, *OpC3* shows the highest value, very slightly exceeding *OpC1*, while *OpC2* presents a marginally lower melting rate during the early stage. By 5 h (18,000 s), all three optimized cases achieve complete melting (liquid fraction = 1), confirming their highly efficient thermal performance and complete use of the PCM's storage capacity. In contrast, the core case exhibits significantly slower melting behavior. At 2.5 h, its liquid fraction is only 0.262, indicating that less than 27% of the PCM has melted. Even after 5 h, the liquid fraction reaches only 0.505, meaning that approximately half of the PCM remains unmolten. This substantial delay clearly highlights the poor heat transfer performance of the core case, which comprises only the HTF tubes and the outer hexagonal shell, without the inner hexagonal frames and bases.

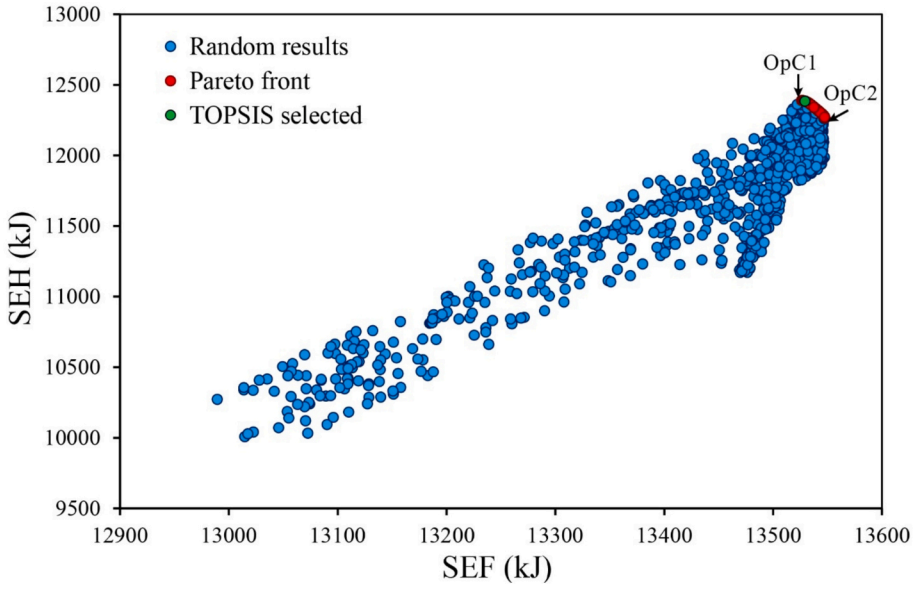

Fig. 7. Pareto fronts for simultaneous maximization of SEH and SEF.

Table 7
Comparison between ANN and numerical findings for the optimized cases (OpC1, OpC2, and OpC3) and the corresponding prediction errors.

Design symbol	Predicted results (kJ)		Numerical results (kJ)		Error (%)	
	SEH	*SEF*	*SEH*	*SEF*	*SEH*	*SEF*
OpC1	12,386	13,525	12,387	13,526	0.009	0.007
OpC2	12,019	13,548	12,085	13,539	0.546	0.066
OpC3	12,384	13,529	12,382	13,528	0.008	0.007

Quantitatively, at 2.5 h, *OpC1*, *OpC2*, and *OpC3* increase the liquid fraction by approximately 254%, 242%, and 255%, respectively, compared to the core case. At 5 h, achieving complete melting instead of 50.5% corresponds to an improvement of nearly 98%. These remarkable enhancements confirm that incorporating the inner hexagonal frames and optimized geometric parameters dramatically strengthen heat transfer pathways, accelerate phase change, and significantly improve the overall charging performance of the TSD. The exact times required to reach half melting (liquid fraction = 0.5) and full melting (liquid fraction = 1) for the optimized configurations have been extracted from the numerical results as follows:

* *OpC1* reaches half melting at 4105 s and full melting at 11732 s
* *OpC2* reaches half melting at 4186 s and full melting at 14123 s
* *OpC3* reaches half melting at 4121 s and full melting at 12143 s

Fig. 8b shows the E_m plots over time for the optimized cases. All three optimized configurations follow nearly identical trends: (1) A rapid increase in E_m during the early charging period, (2) A peak value of approximately 353–365% around 3300 s, and (3) A gradual decline afterward as melting progresses and temperature gradients decrease. *OpC1* and *OpC3* show slightly higher melting enhancement ratios than *OpC2* during the early stage, consistent with their faster melting rates observed in Fig. 8a. The high initial E_m values confirm that geometric optimization significantly intensifies early-stage heat transfer, which is critical for practical charging processes.

In Fig. 8c, the optimized designs show very similar temperature profiles. During the initial heating phase, the PCM temperature increases quickly and then slowly approaches approximately 333.15 K by 5 h. The core case, in contrast, reaches only about 320.54 K in 5 h. The higher temperature rise in the optimized designs indicates: faster sensible heating before melting, more effective latent heat absorption during phase change, and amended overall heat distribution within the PCM domain. The nearly identical temperature curves of *OpC1* and *OpC3* again confirm that the TOPSIS-selected solution (*OpC3*) maintains the strong thermal performance of the single-objective *SEH*-maximized design (*OpC1*), while *OpC2* exhibits only slightly lower early-stage heating rates. In Fig. 8c, the PCM average temperature curves of the optimized cases exhibit a noticeable plateau region between approximately 6000 s and 11,000 s. This plateau corresponds to the dominant phase-change period, during which the input thermal energy is chiefly consumed as latent heat instead of increasing the PCM's sensible temperature. Physically, once the PCM reaches its melting temperature, further heat input does not significantly increase the average temperature. Instead, the energy is consumed to overcome intermolecular forces and convert the solid phase into a liquid. As a result, the temperature remains nearly constant despite continuous heat supply. The slight upward trend in this region is due to partial sensible heating of already melted PCM and local temperature gradients, but the overall slope remains much smaller than during the initial heating stage. In contrast, the core case shows a slower temperature rise and a less pronounced plateau because melting progresses much more gradually. The optimized designs enter and complete the phase-change region earlier, demonstrating enhanced heat transfer performance.

Fig. 8d clearly highlights the superiority of the optimized geometries throughout the charging process. At 2.5 h (9000 s), the contrast is striking. *OpC1* stores 12,387 kJ, *OpC2* stores 12,085 kJ, and *OpC3* stores 12,382 kJ, whereas the Core case stores only 4481 kJ. At this intermediate stage, *OpC1* and *OpC3* exhibit nearly identical performance, and both significantly outperform *OpC2*, although all optimized cases dramatically exceed the Core case. In relative terms, the improvement compared to the Core case is approximately 176% for *OpC1*, 170% for *OpC2*, and 176% for *OpC3*. These results confirm that the optimized geometries substantially accelerate the energy storage process during the early charging period, enabling much faster heat absorption and distribution within the domain. By 5 h (18,000 s), the total stored energy continues to increase and begins to converge among the optimized configurations. *OpC1* stores 13,526 kJ, *OpC2* stores 13,539 kJ, and *OpC3* stores 13,528 kJ, while the Core case reaches only 7621 kJ. At this later stage, all optimized cases achieve nearly identical final storage capacities, slightly exceeding 13.5 MJ. Compared to the Core case, the improvements remain significant, at approximately 77.5% for *OpC1*,

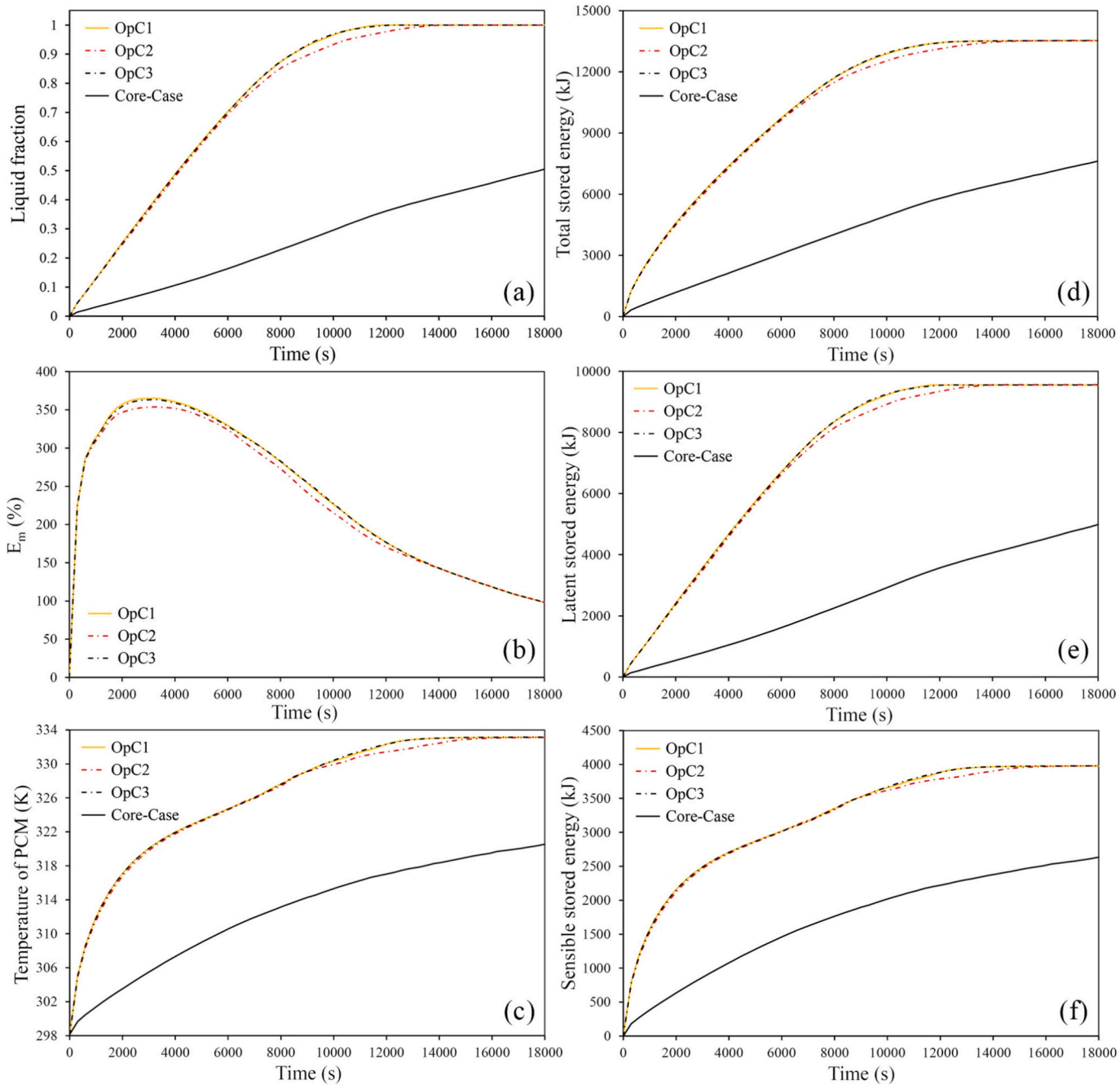

Fig. 8. Time-dependent comparison of the thermal performance of the optimized cases (OpC1, OpC2, and OpC3) and the core case configuration.

77.7% for *OpC2*, and 77.6% for *OpC3*. Although the differences in final stored energy among the optimized cases are minimal, the primary distinction lies in their charging dynamics. *OpC1* and *OpC3* demonstrate faster energy accumulation during the early stage, while *OpC2* shows a marginal advantage in long-term energy accumulation, ultimately reaching the highest final value, albeit by a very small margin. The substantial performance gap between the optimized configurations and the Core case confirms that the incorporation of inner hexagonal frames, bases, and carefully tuned geometric parameters significantly enhances both conductive and convective heat transfer pathways. This structural optimization improves thermal penetration and reduces resistance to heat flow, resulting in markedly higher total stored energy and a much more efficient charging process overall. Fig. 8e shows the evolution of latent stored energy. The optimized cases rapidly accumulate latent heat, reaching near-maximum values before 14,000 s, consistent with the earlier completion of melting observed in Fig. 8a. The core case displays a much slower latent energy growth due to delayed melting. Fig. 8f illustrates sensible stored energy. During the early stage, sensible energy increases rapidly as the PCM temperature approaches the melting point. After melting becomes dominant, the growth rate decreases. The optimized cases maintain consistently higher sensible energy values than the core case, again reflecting enhanced thermal transport mechanisms.

Fig. 9 presents contour plots of the liquid fraction distribution at different times, offering spatial insight into the melting mechanisms. In the core case, melting initiates around the HTF tubes and progresses slowly outward. Large unmolten regions remain even at later times (10,800 s and 14,400 s), particularly in peripheral and lower regions influenced by gravity. The absence of inner hexagonal frames results in weak heat spreading, limited conduction paths, and uneven melting

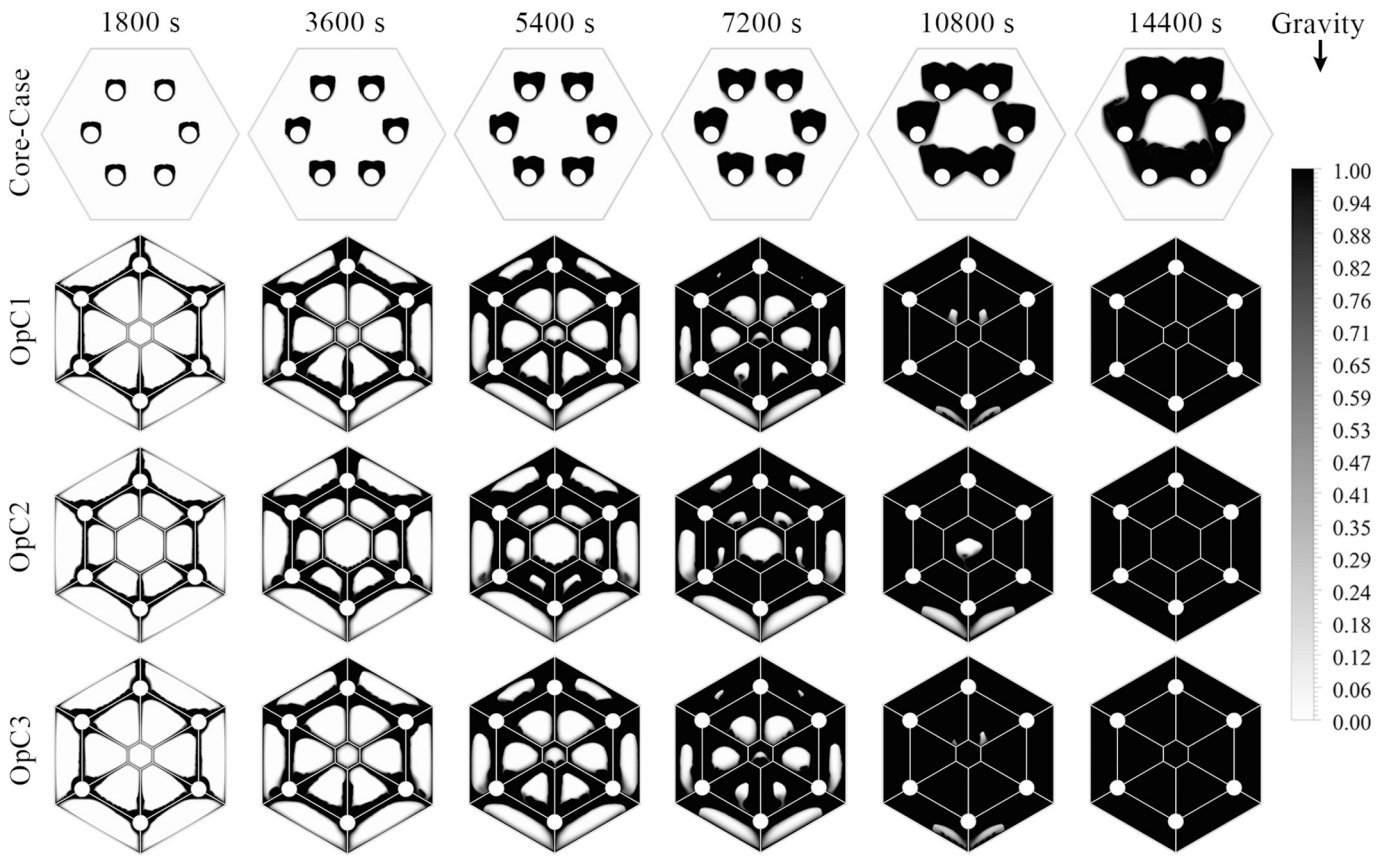

Fig. 9. Temporal evolution of liquid fraction contours for the core case, OpC1, OpC2, and OpC3 at selected charging times.

fronts. In contrast, the optimized cases (*OpC1*, *OpC2*, and *OpC3*) show significantly more uniform and accelerated melting patterns. The presence of inner hexagonal frames and bases enhances heat conduction from the HTF tubes to the PCM mass. The geometry enlarges the effective heat transfer surface and creates multiple radial conduction pathways. *OpC1* and *OpC3* exhibit highly symmetric, rapid melting. Their inner hexagonal structures are configured to provide strong radial heat spreading, resulting in nearly complete melting by 10,800 s. *OpC2*, with a different inner-hexagon configuration, shows marginally slower melting in some regions, particularly near the center at intermediate times. This corresponds with its slightly lower early-stage liquid fraction observed in Fig. 8a. Longer or better-positioned second hexagonal frames improve conductive bridging and reduce thermal resistance, enabling faster energy penetration into PCM regions distant from the tubes.

The optimization results reveal that all three optimal configurations (*OpC1*, *OpC2*, and *OpC3*) converge to the same inclination angle of 30°, indicating that the thermal performance of the storage unit is enhanced when the system is positioned on a vertex rather than resting on a flat side. From a heat transfer perspective, this orientation promotes stronger buoyancy-driven natural convection within the molten PCM. When the system is inclined, the internal flow paths become longer and more vertically oriented, allowing the lighter molten PCM to rise and the cooler PCM to descend over a greater distance. Consequently, the thermosyphon mechanism becomes more active, enhancing heat transport throughout the storage domain. In contrast, when the system lies on one of its flat sides, the available vertical distance for buoyancy-driven circulation is reduced, resulting in weaker natural convection and slower melting. The differences between *OpC1*, *OpC2*, and *OpC3* arise primarily from variations in the lengths of the first and second hexagons, which directly influence the distribution of conductive pathways and the placement of the HTF tubes. In *OpC1* and *OpC3*, the first hexagon length is equal to 30 mm, whereas in *OpC2* it increases to 58.760 mm. A smaller first hexagon concentrates the internal conductive structure closer to the center of the storage unit, creating a denser network of heat transfer pathways in the core region. This arrangement facilitates faster heat penetration into the central PCM zones, thereby accelerating the melting process and increasing energy absorption during the early charging stage. This explains why *OpC1* and *OpC3* exhibit superior short-term thermal performance compared with *OpC2*. Another important distinction is related to the second hexagon length. In *OpC1*, the second hexagon is larger than in *OpC2*, causing the HTF tubes to be positioned closer to the outer shell. As a result, heat transfer is concentrated in the peripheral regions, allowing rapid energy delivery to a specific portion of the PCM domain and promoting faster charging at intermediate times. Conversely, *OpC2* exhibits a more evenly distributed arrangement of hexagonal layers and heat transfer surfaces. This more balanced distribution leads to slightly slower initial melting but provides a more uniform thermal field over extended charging periods. The differences in PCM mass also contribute to the final performance. The PCM masses are 56.83 kg for *OpC1*, 56.90 kg for *OpC2*, and 56.85 kg for *OpC3*. Although the differences are small, the slightly larger PCM volume in *OpC2* contributes to its marginally higher final stored energy at the end of the charging process. *OpC3* represents an intermediate configuration between *OpC1* and *OpC2* and is therefore selected as the optimal compromise design. It retains the same first-hexagon length as *OpC1*, preserving the enhanced conductive pathways toward the center of the storage domain. However, its second hexagon is slightly smaller, causing the HTF tubes to move somewhat inward from the outer shell toward the central region. This adjustment creates a more balanced distribution of heat transfer surfaces while simultaneously providing a slightly larger PCM volume than *OpC1*. Consequently, *OpC3* combines the rapid early-stage charging characteristics of *OpC1* with the strong long-term energy storage capability of *OpC2*, making it the most balanced and practically

attractive design identified in this study.

The introduction of the internal hexagonal frameworks and connecting bases occupies part of the storage volume that would otherwise be filled with PCM. As a result, the PCM mass in the optimized configurations is slightly lower than that of a simple enclosure without these internal structures. From a purely volumetric perspective, this may appear disadvantageous. However, the effectiveness of a latent thermal energy storage system should not be evaluated solely based on PCM quantity, but rather on the extent to which the stored PCM can be actively utilized during the charging process. This trade-off becomes evident when comparing the optimized configurations with the core case. In the core case, the same HTF tubes are present, but the internal hexagonal structures and bases are absent. Consequently, the PCM volume is larger. Nevertheless, despite containing more PCM, the core case exhibits significantly poorer thermal performance, reaching a liquid fraction of only 0.262 after 2.5 h and 0.505 after 5 h, whereas all optimized configurations achieve complete melting within the same charging period. This demonstrates that simply increasing PCM volume does not guarantee superior energy storage performance. A large portion of the PCM in the core case remains unmolten and therefore cannot effectively contribute to thermal energy storage. In practical terms, PCM that cannot be adequately charged represents underutilized storage capacity. The added bases perform several important functions that justify the reduction in PCM volume. First, they act as additional conductive pathways, extending heat transfer from both the HTF tubes and the outer shell into regions that would otherwise experience delayed melting. Second, they improve the utilization of the available PCM by accelerating melting and reducing thermally inactive zones. Third, the bases mechanically connect the HTF tubes to the shell, creating a fully integrated structure. This integration simplifies the overall design and reduces the thermal contact resistance that would otherwise exist between separately manufactured components. As a result, heat can be transferred more efficiently from the HTF channels into the storage domain. It is also acknowledged that the proposed design requires additional construction material compared to the core case. However, the substantial gains in charging performance and stored energy far outweigh the modest reduction in PCM volume and the increase in material usage. The results demonstrate that improving PCM utilization is more beneficial than merely maximizing PCM quantity. Therefore, the proposed configuration achieves a favorable balance between storage capacity, heat transfer enhancement, structural integrity, and practical performance.

Fig. 10 illustrates the transient thermal behavior of the hexagonal system under four different configurations. In the Core Case, the temperature field initially exhibits strong localization around the internal heat-generating elements, as shown by the bright yellow regions at 1800 s. The surrounding domain remains relatively cold (blue to purple), indicating steep thermal gradients and limited heat diffusion. As time progresses to 3600 s and 5400 s, thermal plumes expand outward from each source, gradually merging toward the center. By 7200 s and beyond, the interaction between adjacent thermal fronts becomes more pronounced, and buoyancy effects induced by gravity cause an upward distortion of the temperature field. At later times (10,800 s and 14,400 s), the domain approaches a more uniform, elevated temperature distribution, although residual gradients persist near the boundaries and around the heat sources. In contrast, the optimized cases (*OpC1*, *OpC2*, and *OpC3*) demonstrate a more distributed and balanced heat transfer process from the early stages. At 1800 s, the temperature contours already show a more extensive thermal footprint than in the Core Case, suggesting enhanced conductive or convective transport pathways. As time advances, the thermal gradients diminish more rapidly, and the hot regions spread more uniformly across the hexagonal domain. Particularly after 7200 s, the optimized configurations exhibit a smoother, more homogeneous temperature field with fewer localized hot spots. By 10,800 s and 14,400 s, the entire domain in these cases becomes nearly isothermal, indicating improved thermal management and more effective heat dissipation. Among the optimized designs, subtle differences can be observed in the rate of homogenization and the symmetry of the temperature contours. Still, all three outperform the Core Case in reducing peak temperature concentration and accelerating thermal uniformity. The influence of gravity is evident in the slight vertical asymmetry of the contours at intermediate times, especially in the Core

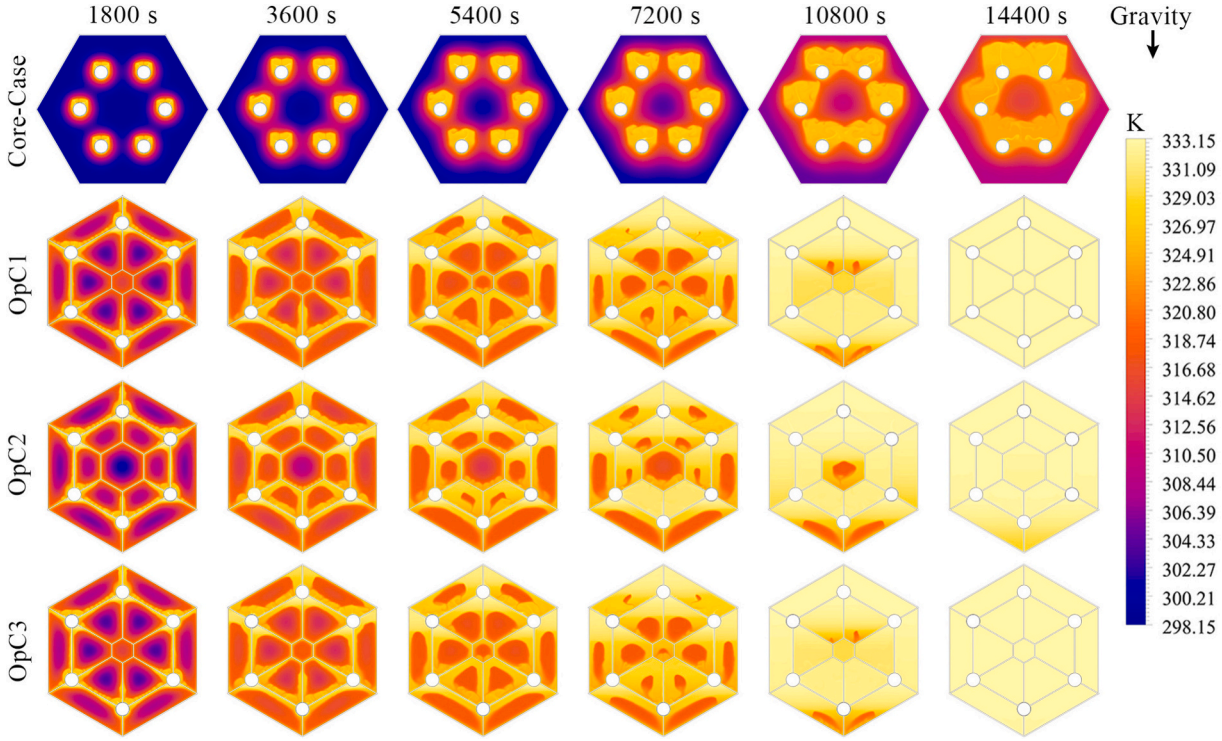

Fig. 10. Temperature contours within the hexagonal domain for the Core Case and three optimized configurations (OpC1, OpC2, and OpC3).

Case. In contrast, the optimized cases mitigate this effect by promoting more evenly distributed heat transport.

8. Fabrication and manufacturability

In TSDs, one of the main engineering challenges is ensuring proper sealing, particularly at the interfaces between the storage container and the inlet/outlet connections of the HTF. In the present design, the internal structure, consisting of the concentric hexagonal containers and bases is integrated as a single monolithic unit within the outer shell. This integration reduces the number of joints and interfaces, which are typically the primary sources of leakage in modular systems. From a manufacturing perspective, such a monolithic structure can be produced using various fabrication techniques, including casting or molding methods, which are relatively cost-effective for producing complex geometries in a single piece. After the primary fabrication stage, only the connection regions (e.g., inlet and outlet ports) require high-precision machining. These regions can be finished using CNC machining to ensure tight tolerances and reliable sealing. This approach minimizes the need for multiple assembled components and reduces cumulative manufacturing errors. In terms of cost, although the internal honeycomb-inspired geometry (hexagonal layers and bases) introduces some geometric complexity, the overall system can still be economically competitive. This is because modular systems, which consist of multiple assembled parts, often require additional sealing components, welding, fastening, and quality control steps, all of which increase cost and potential failure points. In contrast, the proposed integrated design reduces assembly steps, which can offset the added geometric complexity. Regarding mechanical integrity, the structure benefits from the well-known strength of honeycomb architectures, which are widely recognized for their high stiffness-to-weight ratio and structural robustness. The internal bases not only enhance heat transfer but also act as reinforcing elements, improving the structural stability of the system under thermal expansion and operational stresses. It should also be acknowledged that the inclusion of internal bases and multiple hexagonal layers does increase fabrication complexity to some extent, which may slightly raise manufacturing costs compared to very simple geometries. However, this is balanced by the advantages of improved performance, reduced leakage risk, and fewer assembly requirements. Overall, the proposed design is practically feasible using current manufacturing technologies, particularly for applications where performance, durability, and reliability are prioritized.

9. Comparison with previous thermal energy storage studies

Table 8 presents a comparison between the proposed honeycomb shell-and-tube thermal energy storage (TES) system and selected studies reported in the literature. The comparison includes different storage geometries, PCMs, operating temperature differences, and charging times required to achieve a high melting level (liquid fraction $\varphi \geq 0.9$). The results indicate that the proposed honeycomb-inspired design achieves a charging time of 12,050 s with a temperature difference of 9 K using RT50 PCM. Although some fin-enhanced configurations reported shorter charging times, such as those of Cui et al. [44] (1166 s), Ran et al. [45] (1619 s), and Saini et al. [46] (1747 s), these systems generally employ extensive fin structures or operate under different geometric and thermal conditions, which may increase manufacturing complexity, material consumption, and pressure-drop-related issues. Compared with conventional shell-and-tube TES systems, the proposed design demonstrates competitive performance. For example, charging times reported by Li et al. [25], Deng et al. [47], and Vafaei et al. [48] are 13,592 s, 10637 s, and 14,700 s, respectively, while operating under similar or higher temperature differences. The main novelty of the present work lies not only in the achieved charging performance but also in the integration of a bio-inspired honeycomb shell-and-tube geometry optimized through a multi-objective GA framework. Unlike most previous studies that focus primarily on fin arrangements or single-objective thermal enhancement, the present study simultaneously considers geometric optimization and thermal performance enhancement. The results demonstrate that the honeycomb architecture provides an effective balance between heat transfer enhancement and structural simplicity, making it a promising alternative for latent heat thermal energy storage applications.

Table 8
Comparison of the present honeycomb-inspired thermal energy storage system with selected TES studies reported in the literature in terms of storage configuration, PCM type, thermal operating conditions, and charging performance.

Study	Design of thermal storage	PCM	T_{HTF}-$T_{liquid\ PCM}$ (K)	Time for $\varphi \geq 0.9$ (s)
This study	Honeycomb shell-and-tube heat exchangers	RT50	9	12,050
Li et al. [25]	Shell-and-tube TES	RT50	14	13,592
Saini et al. [46]	LHS with lotus-shaped fins	RT82	4.99	1747
Niketan et al. [49]	LHTES with X-shaped fins	Pentaerythritol	36.85	9560
Saini et al. [50]	Cesaro fin-based LHS	RT82	4.99	2564
Al-Abidi et al. [51]	TTHE	RT82	5	2220
Ghalambaz et al. [52]	Shell-and-tube TES	Coconut oil	25.85	22,709
Nekahi et al. [53]	Honeycomb-structured shell-and-tube TES	RT50	9	5150
Xu et al. [54]	TTHE	RT60	10	2550
Yan et al. [55]	Compact-TES with ribs	RT42	23	9003
Vaferi et al. [48]	TES tank	RT50	19	14,700
Vaferi et al. [56]	Modular-LHS	Lauric acid	11.8	17,775
Cui et al. [44]	TTHE with radial fins	RT50	24	1166
Zheng et al. [57]	Compact-LHS with fins	RT42	11.1	10,880
Gurel et al. [58]	P-LHS	n-octadecane	33.65	2100
Deng et al. [47]	Multi-section LHS	RT50	14	10,637
Ran et al. [45]	TTHE with fins	Lauric acid	21.8	1619
Vogel et al. [59]	Finned-LHS	NaNo3	10	5400
Esmaeili et al. [60]	TTHE with tree-shaped fins	RT82	5	2416

10. Conclusions

This study introduced and systematically evaluated a configuration-oriented enhancement strategy for latent thermal energy storage devices by developing a novel hexagonal PCM structure. By integrating concentric hexagonal frameworks, bases, embedded HTF tubes, and a monolithic outer shell, the proposed design effectively addressed the limitations of low PCM thermal conductivity and weak natural convection. The geometric parameters (*FL*, *SL*, and θ) were selected based on their physical impact on heat transfer mechanisms and optimized using an ANN–GA multi-objective framework. All reported results, including melting behavior, stored energy, optimization outcomes, and performance comparisons, were obtained from numerical simulations. The following results demonstrated that:

* The developed ANN model (3–6–2 architecture) achieved excellent predictive accuracy, confirmed by very high R^2 and low RMSE

values. Among the design variables, *SL* was identified as the most influential parameter governing stored energy, while *FL* and θ showed comparatively smaller effects at intermediate times.

* Single-objective optimization yielded two distinct optimal designs: *OpC1* (*FL* = 30 mm, *SL* = 137.140 mm, $\theta = 30^{\circ}$) for maximizing stored energy at 2.5 h, and *OpC2* (*FL* = 58.760 mm, *SL* = 128.140 mm, $\theta = 30^{\circ}$) for maximizing stored energy at 5 h. Multi-objective optimization combined with the TOPSIS method identified a balanced solution, *OpC3* (*FL* = 30 mm, *SL* = 135.549 mm, $\theta = 30^{\circ}$), which provides a compromise between *SEH* and *SEF*.
* At 2.5 h, the liquid fraction reached approximately 0.93 for the optimized cases, compared with 0.262 for the Core case, representing an improvement of up to 255%. By 5 h, all three optimized cases achieved complete melting (liquid fraction = 1), representing an improvement of nearly 98% relative to the core case.
* At 2.5 h, the optimized configurations stored approximately 12,000 kJ, whereas the Core case stored only 4481 kJ. The improvement was approximately 170% compared to the Core case. By 5 h, the optimal cases stored about 13,500 kJ, while the Core case reached only 7621 kJ. Compared to the Core case, the improvements remained significant, at approximately 77.5%.
* Among the optimized designs, *OpC3* exhibited performance consistently between *OpC1* and *OpC2*, combining rapid early-stage energy absorption with high final storage capacity. This balanced behavior makes *OpC3* the most suitable and practically optimal configuration identified in this study.

Furthermore, the design-related considerations presented below should be regarded as recommendations for future work rather than validated findings. In this regard, it is suggested that the storage capacity can be further enhanced by arranging two or more hexagonal containers in series, allowing for a larger PCM volume while maintaining efficient charging performance. However, it should be noted that extending the system length can result in a decrease in HTF thermal energy along the flow path. To compensate for this effect, a higher HTF flow rate may be required to maintain adequate heat-transfer performance throughout the system. The reported findings are based on two-dimensional numerical simulations coupled with ANN-GA optimization conducted within the selected ranges of design and operating parameters. The identified optimal configurations and performance improvements are therefore valid within the investigated parameter space. Although the numerical model was carefully validated and the proposed honeycomb-inspired geometry demonstrated promising thermal performance, direct experimental validation of the optimized hexagonal thermal energy storage configuration has not yet been performed. Experimental investigations are therefore recommended as an important direction for future work to verify the numerical predictions and assess the practical feasibility, manufacturability, and long-term operational performance of the proposed design under real operating conditions.

CRediT authorship contribution statement

Yonghui Li: Investigation, Data curation. **Ali Basem:** Formal analysis, Data curation. **Haibo Zhang:** Supervision, Investigation. **Mohamed Arbi Khlifi:** Writing – original draft, Formal analysis. **Hyder H. Abed Balla:** Writing – review & editing, Supervision, Investigation. **Mohammad Nadeem Khan:** Validation, Data curation. **Hanaa Abu-Zinadah:** Writing – review & editing, Investigation. **Farkhod Rakhmonov:** Writing – review & editing, Writing – original draft. **Yasser Fouad:** Supervision, Project administration, Methodology, Funding acquisition, Conceptualization. **Ibrahim Mahariq:** Writing – review & editing, Validation, Supervision, Resources.

Declaration of competing interest

The authors declare that they have no known competing financial interests or personal relationships that could have appeared to influence the work reported in this paper.

Acknowledgements

Ongoing Research Funding Program, (ORF-2026-698), King Saud University, Riyadh, Saudi Arabia. This work was financially supported by the Key Project of Philosophy and Social Sciences in Yunnan Province: "Research on Rule Coordination and Governance Innovation in China-Myanmar Cross-Border Data Flow (ZD202525)"; the National Social Science Foundation Project of China (23BJL088).

Data availability

The authors do not have permission to share data.

References

[1] Y. Yuan, Y. Zhang, S. Shi, X. Wang, H. Guo, W. Zhou, et al., Research progress on phase change heat storage exchangers for solar thermal utilization, Sol. Energy Mater. Sol. Cells 295 (2026) 113987, https://doi.org/10.1016/j.solmat.2025.113987.
[2] S. Yin, X. Yan, X. Fu, Z. Liu, A solar integrated adsorption carbon dioxide energy storage system, Energy Convers. Manag. 347 (2026) 120573, https://doi.org/10.1016/j.enconman.2025.120573.
[3] Z. Song, H. Jia, T. Gao, Y. Yu, Topology optimization investigation on thermal performance of phase change materials in heat storage unit with elliptic tube, J. Energy Storage 143 (2026) 119661, https://doi.org/10.1016/j.est.2025.119661.
[4] G. Xia, X. He, Y. Jia, Y. Zhu, Z. Tian, Design of a Cylindrical Thermal Rotary Concentrator Based on transformation thermodynamics, Materials (Basel) 18 (2025) 4440, https://doi.org/10.3390/ma18194440.
[5] F.L. Rashid, S.A. Kadhim, A. Bouabidi, M.K. Abdalrahem, M.A. Al-Obaidi, A. M. Ashour, et al., Recent advances of solar dryer with energy storage: a comprehensive review, J. Stored Prod. Res. 115 (2026) 102820, https://doi.org/10.1016/j.jspr.2025.102820.
[6] K. Tang, X. Zhang, Y. Tang, T. Li, S. Wu, Advanced thermal energy storage technologies for vehicle thermal management: emerging applications, challenges, and future prospects, Renew. Sust. Energ. Rev. 235 (2026) 116964, https://doi.org/10.1016/j.rser.2026.116964.
[7] M.B.M. Christensen, J. Alexandersen, Topology optimisation of heat sinks embedded with phase-change material for minimising temperature oscillations, Computation 14 (2026) 23, https://doi.org/10.3390/computation14010023.
[8] S.A. Abdollahi, A. Basem, A. Alizadeh, D.J. Jasim, M. Ahmed, A.J. Sultan, et al., Combining artificial intelligence and computational fluid dynamics for optimal design of laterally perforated finned heat sinks, Results Eng. 21 (2024) 102002, https://doi.org/10.1016/j.rineng.2024.102002.
[9] U. Srivastava, R.R. Sahoo, Advanced fin designs for enhancement in thermal management of eutectic phase change materials in a latent heat thermal energy storage system, Int. Commun. Heat Mass Transf. 170 (2026) 109932, https://doi.org/10.1016/j.icheatmasstransfer.2025.109932.
[10] M. Arslan, S. Mehdi, X. Duan, H.M. Ali, Bio-based phase change materials: a sustainable revolution in thermal energy storage and management, Int. Commun. Heat Mass Transf. 175 (2026) 111118, https://doi.org/10.1016/j.icheatmasstransfer.2026.111118.
[11] A. Castro-Vizcaíno, M.S. Romero-Cano, J.L. Bosch, M.J. Ariza, J. Alonso-Montesinos, A.M. Puertas, et al., Performance of a thermal energy storage tank based on latent heat with different capsule allocations. Experimental study in a pilot facility, J. Energy Storage 141 (2026) 119282, https://doi.org/10.1016/j.est.2025.119282.
[12] J. Wang, W. Luo, M. Zou, W. Chen, G. Zhu, S. Tan, et al., Ultra-flexible, adaptable and multifunctional polymer-based composite phase change materials for full-stage battery thermal management, Compos. Part B Eng. 313 (2026) 113416, https://doi.org/10.1016/j.compositesb.2026.113416.
[13] R.K. Padhy, K. Suresh, A. Chandrasekhar, TOMATOES: topology and material optimization for latent heat thermal energy storage devices, Appl. Energy 406 (2026) 127322, https://doi.org/10.1016/j.apenergy.2025.127322.
[14] Y. Yan, H. Zhang, F. Yang, Y. Xu, Z. Ge, Y. Wu, et al., Assessment of low-GWP refrigerants in ultra-high-temperature transcritical heat pumps: a systematic evaluation framework based on life-cycle economics, Appl. Therm. Eng. 291 (2026) 130083, https://doi.org/10.1016/j.applthermaleng.2026.130083.
[15] A. Vaisi, M.M. Soltani, M.F. Abdollahi, M. Gorji-Bandpy, M.A. Haghghi, Experimental thermal–hydraulic evaluation and correlation development of geometrically modified wire-matrix turbulators in the tube side of double-pipe heat exchangers, Case Stud. Therm. Eng. 82 (2026) 108020, https://doi.org/10.1016/j.csite.2026.108020.
[16] Y. Yang, K. Zhang, L. Wang, Q. Zhang, K. Song, G. Shi, Investigation on the thermal performance of honeycomb bionic fin latent heat thermal energy storage units, Int. J. Therm. Sci. 220 (2026) 110333, https://doi.org/10.1016/j.ijthermalsci.2025.110333.
[17] S. Tang, D. Zhang, W. Wang, H. Xi, X. Wu, M. Guo, Enhancing melting-solidification performance of latent heat thermal energy storage units with twisted

fins, Renew. Energy 260 (2026) 125250, https://doi.org/10.1016/j.renene.2026.125250.
[18] S. Pal, D. Bhanja, R.D. Misra, Simulation on PCM melting improvement with triple-finned horizontal shell-tube latent-heat thermal energy storage unit: effect of fin size and distribution, J. Energy Storage 134 (2025) 118195, https://doi.org/10.1016/j.est.2025.118195.
[19] B. Kamkari, A.M. Nair, R.V. Ravindran, D. Cotter, C. Wilson, N.J. Hewitt, Biomimetic fractal fins for enhanced thermal performance in fin-and-tube latent heat energy storage, J. Energy Storage 149 (2026) 120050, https://doi.org/10.1016/j.est.2025.120050.
[20] M.L. Benlekkam, B. Allam, M. Arıcı, Effect of Y-shaped fin geometry on thermal performance of LHTES: a numerical investigation, Int. Commun. Heat Mass Transf. 172 (2026) 110423, https://doi.org/10.1016/j.icheatmasstransfer.2025.110423.
[21] J. Li, X. Chen, J. Shen, Y. Zhang, D. Liu, Optimal heat storage temperature and performance of ORC-based Carnot battery at various application scenarios, Energy Convers. Manag. 318 (2024) 118906, https://doi.org/10.1016/j.enconman.2024.118906.
[22] Y. Zhang, J. Li, M. Yu, X. Chen, X. Chen, J. Shen, Dominant factor identification and fast optimization of Carnot battery by integrating SHAP and physics-guided neural network, Appl. Energy 401 (2025) 126641, https://doi.org/10.1016/j.apenergy.2025.126641.
[23] G. Liu, S. Zhang, Y. Chen, L. Pu, Performance improvement of a novel plate-finned latent thermal energy storage system by numerical simulation, artificial neural network, and genetic algorithm, Appl. Therm. Eng. 287 (2026) 129450, https://doi.org/10.1016/j.applthermaleng.2025.129450.
[24] J.-B. Mao, A. Basem, H.H. Abed Balla, O.J. Alkhatib, Y. Elmasry, Y. Li, et al., Triangular-rib structural mastery for enhanced latent heat storage system: artificial neural network optimization of geometry, orientation, and cost-effectiveness, J. Energy Storage 152 (2026) 120463, https://doi.org/10.1016/j.est.2026.120463.
[25] Y. Li, A. Basem, S. Alhumaid, R. Ghandour, Z. Bayhan, X. Li, et al., Performance-cost co-optimization of shell-and-tube thermal energy storage units with enhanced sub-fin geometry via a hybrid numerical–AI approach, J. Energy Storage 144 (2026) 119655, https://doi.org/10.1016/j.est.2025.119655.
[26] S. Sharma, N. Sellami, A.A. Tahir, T.K. Mallick, R. Bhakar, Performance improvement of a CPV system: experimental investigation into passive cooling with phase change materials, Energies 14 (2021) 3550, https://doi.org/10.3390/en14123550.
[27] E. Paccha-Herrera, W.R. Calderón-Muñoz, M. Orchard, F. Jaramillo, K. Medjaher, Thermal Modeling approaches for a LiCoO2 Lithium-ion battery—a comparative study with experimental validation, Batteries 6 (2020) 40, https://doi.org/10.3390/batteries6030040.
[28] C. Dong, G. He, Z. Meng, S. Asim, D. Li, Y. Hu, Optimality criterion-based latent heat storage heat exchangers topology optimization method, J. Energy Storage 125 (2025) 117012, https://doi.org/10.1016/j.est.2025.117012.
[29] Z. Chen, X. Li, L. Chen, N. Huang, L. Liu, P. Du, et al., Parametric study and thermal-dynamic analysis on angles of leading bifurcations in double-layer microchannel heat sinks with nested impacting jet structure, Int. Commun. Heat Mass Transf. 175 (2026) 110945, https://doi.org/10.1016/j.icheatmasstransfer.2026.110945.
[30] X. Xu, Q. Yu, B. Shi, Y. Tan, G. Zhang, J. Zhang, et al., Study on the thermal storage performance of bio-inspired fin structures in latent heat energy storage system with optimized phase change materials, Appl. Therm. Eng. 268 (2025) 125850, https://doi.org/10.1016/j.applthermaleng.2025.125850.
[31] K.A. Hammoodi, H.A. Hasan, M.H. Abed, A. Basem, A.M. Al-Tajer, Control of heat transfer in circular channels using oblique triangular ribs, Results Eng. 15 (2022) 100471, https://doi.org/10.1016/j.rineng.2022.100471.
[32] L. Ye, T. Zheng, X. Wang, X. Liang, C. Liu, Evaluating the heat transfer characteristics of mesh-fed slot cooling configuration: influence of slot height and pin-fin arrangement, Appl. Therm. Eng. 271 (2025) 126304, https://doi.org/10.1016/j.applthermaleng.2025.126304.
[33] X. Huang, Z. Du, Z. Liu, X. Yang, B. Sundén, Research progress of fin design in latent heat energy storage enhancement technology, Appl. Therm. Eng. 278 (2025) 127157, https://doi.org/10.1016/j.applthermaleng.2025.127157.
[34] E. Revello, P. Dixit, K. Turunen, A. Santasalo-Aarnio, A.H.A. Monteverde, Assessment of phase change materials for thermal energy storage in battery systems for heavy-duty vehicle applications, Energy Convers. Manag. 349 (2026) 120816, https://doi.org/10.1016/j.enconman.2025.120816.
[35] N. Kousha, M. Rahimi, R. Pakrouh, R. Bahrampoury, Experimental investigation of phase change in a multitube heat exchanger, J. Energy Storage 23 (2019) 292–304, https://doi.org/10.1016/j.est.2019.03.024.
[36] F. Agyenim, P. Eames, M. Smyth, Heat transfer enhancement in medium temperature thermal energy storage system using a multitube heat transfer array, Renew. Energy 35 (2010) 198–207, https://doi.org/10.1016/j.renene.2009.03.010.
[37] W. Zhao, J. Chen, H. Jiang, M. Li, R. Liu, Y. Gao, et al., TiN supported 3D directional tubular skeleton encapsulating phase change materials for efficient solar-thermal energy conversion and storage, Sol. Energy 302 (2025) 114071, https://doi.org/10.1016/j.solener.2025.114071.
[38] F. Ren, P.-Z. Zhuang, X. Chen, H.-S. Yu, H. Yang, Physics-informed extreme learning machine (PIELM) for Stefan problems, Comput. Methods Appl. Mech. Eng. 441 (2025) 118015, https://doi.org/10.1016/j.cma.2025.118015.
[39] A.W. Kandeal, M. Ismail, A. Basem, M.M. Elsayad, W.H. Alawee, H.S. Majdi, et al., An overview of the improvement of natural convection heat transfer via surface thermal radiation for different geometries, Results Eng. 23 (2024) 102514, https://doi.org/10.1016/j.rineng.2024.102514.
[40] Y. Wang, Q. Guo, Z. Zhou, H. Li, D. Ma, Optimisation investigation on hybrid battery thermal management system for electric aircraft based on genetic algorithm, Eng. Appl. Comput. Fluid Mech. 19 (2025), https://doi.org/10.1080/19942060.2025.2517314.
[41] A. Shafee, A. Basem, AL-bonsrulah HAZ, S. Althobaiti, Mohamed SMY, Thermal management of NEPCM during freezing considering conduction mechanism, J. Therm. Anal. Calorim. 149 (2024) 14355–14371, https://doi.org/10.1007/s10973-024-13717-0.
[42] M. Sheng, H. Rong, C. Zhou, X. Sheng, X. Hu, X. Tang, et al., Simultaneously achieving high energy density, mechanical robustness, and closed-loop recyclability in phase change materials for advanced thermal energy systems, Adv. Energy Mater. (2026), https://doi.org/10.1002/aenm.70874.
[43] F.K. Chowdhury, M.S. Sami, M.J. Alam, A. Sayem, M.M.A. Khan, Machine learning-assisted NSGA-II-TOPSIS optimization of weld strength and processing time in fused deposition modeling, Results Eng. 29 (2026) 109365, https://doi.org/10.1016/j.rineng.2026.109365.
[44] Q. Cui, T. Ning, C. Huang, C. Wu, J. Su, Design and operation of a novel cross fin in hot-water production system for buildings, Buildings 15 (2025) 320, https://doi.org/10.3390/buildings15030320.
[45] L. Ran, G. Yan, V. Goyal, S. Abdullaev, F.M. Alhomayani, L.T. Le, et al., Advancing solar thermal utilization by optimization of phase change material thermal storage systems: a hybrid approach of artificial neural network (ANN)/genetic algorithm (GA), Case Stud. Therm. Eng. 64 (2024) 105513, https://doi.org/10.1016/j.csite.2024.105513.
[46] P. Saini, J.D. Osorio, M.P. Shah, U.N. Patel, A. Nelapudi, L.A. Porto-Hernandez, Nature-inspired lotus-shaped fins combined with hybrid nanoparticles and metal foam for high-performance latent heat thermal energy storage, Int. J. Heat Mass Transf. 255 (2026) 127897, https://doi.org/10.1016/j.ijheatmasstransfer.2025.127897.
[47] W. Deng, J. Li, S. Samad, A.M. Abed, A. Almadhor, S. Alhumaid, et al., Optimization and prediction of heat absorption in a modular multi-section latent heat storage system with dome-shaped components using a multilayer perceptron model, TOPSIS analysis, and pareto fronts, J. Energy Storage 131 (2025) 117542, https://doi.org/10.1016/j.est.2025.117542.
[48] K. Vaferi, S. Nekahi, S. Nekahi, H. Ghaebi, Charging/discharging performance examination in a finned-tube heat storage tank: based on artificial neural network, pareto optimization, and numerical simulation, Case Stud. Therm. Eng. (2025) 106388, https://doi.org/10.1016/j.csite.2025.106388.
[49] Saini P. Niketan, A. Dhar, S. Powar, Parametric optimization and charging performance enhancement of X-fin employed shell and tube solid-solid PCM based latent heat thermal energy storage system, J. Energy Storage 152 (2026) 120356, https://doi.org/10.1016/j.est.2026.120356.
[50] P. Saini, A. Dhar, S. Powar, Parametric optimization of a cesaro fins employed latent heat storage system for melting performance enhancement, J. Energy Storage 51 (2022) 104534, https://doi.org/10.1016/j.est.2022.104534.
[51] A.A. Al-Abidi, S. Mat, K. Sopian, M.Y. Sulaiman, A.T. Mohammad, Internal and external fin heat transfer enhancement technique for latent heat thermal energy storage in triplex tube heat exchangers, Appl. Therm. Eng. 53 (2013) 147–156, https://doi.org/10.1016/j.applthermaleng.2013.01.011.
[52] M. Ghalambaz, Mehryan SAM, A. Hajjar, Shdaifat M.Y. Al, O. Younis, P. Talebizadehsardari, et al., Thermal charging optimization of a wavy-shaped nano-enhanced thermal storage unit, Molecules 26 (2021) 1496, https://doi.org/10.3390/molecules26051496.
[53] S. Nekahi, F.S. Moghanlou, M. Vajdi, K. Vaferi, S. Nekahi, T. Gholizadeh, Development and performance evaluation of a honeycomb-structured shell-and-tube thermal storage system integrating a series of openings on the hexagonal cells for enhanced energy absorption/release, Int. Commun. Heat Mass Transf. 173 (2026) 110897, https://doi.org/10.1016/j.icheatmasstransfer.2026.110897.
[54] H. Xu, N. Wang, C. Zhang, Z. Qu, M. Cao, Optimization on the melting performance of triplex-layer PCMs in a horizontal finned shell and tube thermal energy storage unit, Appl. Therm. Eng. 176 (2020) 115409, https://doi.org/10.1016/j.applthermaleng.2020.115409.
[55] G. Yan, J. Li, R.N. Dara, M. Shaban, R. Ghandour, F.M. Alhomayani, et al., Solar-powered compact thermal energy storage system with rapid response time and rib-enhanced plate via techniques of CFD, ANN, and GA, J. Energy Storage 105 (2025) 114807, https://doi.org/10.1016/j.est.2024.114807.
[56] K. Vaferi, A. Farajollahi, T. Gholizadeh, M. Rostami, Enhancing charging and discharging performance in a novel latent heat storage via design optimization and artificial neural network modeling, J. Energy Storage 114 (2025) 115757, https://doi.org/10.1016/j.est.2025.115757.
[57] Z. Zheng, G. Yan, A.M. Abed, M.A. Alghassab, B. Abdullaeva, F.M. Alhomayani, et al., Optimizing and investigating the charging time of phase change materials in a compact-latent heat storage using pareto front analysis, artificial neural networks, and numerical simulations, J. Energy Storage 102 (2024) 113966, https://doi.org/10.1016/j.est.2024.113966.
[58] B. Gürel, A numerical investigation of the melting heat transfer characteristics of phase change materials in different plate heat exchanger (latent heat thermal energy storage) systems, Int. J. Heat Mass Transf. 148 (2020) 119117, https://doi.org/10.1016/j.ijheatmasstransfer.2019.119117.
[59] J. Vogel, M. Johnson, Natural convection during melting in vertical finned tube latent thermal energy storage systems, Appl. Energy 246 (2019) 38–52, https://doi.org/10.1016/j.apenergy.2019.04.011.
[60] Z. Esmaeili, S.M. Vahidhosseini, S. Rashidi, Enhancing latent heat thermal energy storage in triplex tube heat exchangers using tree-shaped fin structures with novel branching methods, J. Energy Storage 97 (2024) 112970, https://doi.org/10.1016/j.est.2024.112970.